Geochronology and paleoclimatic implications of the last deglaciation of the Mauna Kea Ice Cap, Hawaii

Faron S. Anslow [a], Peter U. Clark [b,*], Mark D. Kurz [c], Steven W. Hostetler [d]

[a] Department of Earth and Ocean Sciences, University of British Columbia, Vancouver, BC V6T 1Z4

[b] Department of Geosciences, Oregon State University, Corvallis, OR 97330

[c] Department of Marine Chemistry and Geochemistry, Woods Hole Oceanographic Institution, Woods Hole, MA 02543

[d] U.S. Geological Survey, Department of Geosciences, Oregon State University, Corvallis, OR 97330

* Corresponding author. Tel: 541-737-1247.

E-mail address: clarkp@onid.orst.edu (P.U. Clark).

Abstract

We present new ^{3}He surface exposure ages on moraines and bedrock near the summit of Mauna Kea, Hawaii, which refine the age of the Mauna Kea Ice Cap during the Local Last Glacial Maximum (LLGM) and identify a subsequent fluctuation of the ice margin. The ^{3}He ages, when combined with those reported previously, indicate that the local ice-cap margin began to retreat from its LLGM extent at 20.5 ± 2.5 ka, in agreement with the age of deglaciation determined from LLGM moraines elsewhere in the tropics. The ice-cap margin receded to a position at least 3 km upslope for ~5.1 kyr before readvancing nearly to its LLGM extent. The timing of this readvance at ~15.4 ka corresponds to a large reduction of the Atlantic meridional overturning circulation (AMOC) following Heinrich Event 1. Subsequent ice-margin retreat began at 14.6 ± 1.9 ka, corresponding to a rapid resumption of the AMOC and onset of the Bølling warm interval, with the ice cap melting rapidly to complete deglaciation. Additional ^{3}He ages obtained from a flood deposit date the catastrophic outburst of a moraine-dammed lake roughly coeval with the Younger Dryas cold interval, suggesting a more active hydrological cycle on Mauna Kea at this time. A coupled mass balance and ice dynamics model is used to constrain the climate required to generate ice caps of LLGM and readvance sizes. The depression of the LLGM equilibrium line altitude requires atmospheric cooling of 4.5 ± 1 ^{o}C, whereas the mass balance modeling indicates an accompanying increase in precipitation of as much as three times that of present. We hypothesize (1) that the LLGM temperature depression was associated with global cooling, (2) that the temperature depression that contributed to the readvance occurred in response to an atmospheric teleconnection to the North Atlantic, and (3) that the precipitation enhancement associated with both events occurred in response to a southward shift in the position of the inter-tropical convergence zone (ITCZ). Such a shift in the ITCZ would

have allowed midlatitude cyclones to reach Mauna Kea more frequently which would have increased precipitation at high elevations and caused additional cooling.

Introduction

Reconstructing climate during the last glacial maximum (LGM, 26,000 to 19,000 years ago; Clark et al., 2009) provides important insights into understanding climate responses to radiative forcing that differed significantly from the present. Although the effects of continental ice sheets, insolation, and atmospheric CO_2 on radiative forcing during the LGM are reasonably well constrained (Broccoli, 2000), oceanic and terrestrial responses of the tropics to this forcing remain uncertain. CLIMAP Project Members (1976, 1981) argued that the LGM sea surface temperatures (SSTs) of large areas of tropical and subtropical oceans were similar (or even warmer) to present, suggesting that the oceans are either insensitive to climate change, or that responses in the tropical oceans lead or lag those of higher latitudes. When CLIMAP SSTs are specified as boundary conditions in climate models, however, model simulations of temperature and precipitation cannot be reconciled with tropical fossil pollen records or with records of former tropical glaciers which indicate that the LGM tropical atmosphere was cooler and somewhat drier than present (Rind and Peteet, 1985; Betts and Ridgway, 1992; Pollard and Thompson, 1997; Pinot et al., 1999; Hostetler and Clark, 2000; Greene et al., 2002; Hostetler et al., 2006). Indeed, there is evidence from other climate proxies that LGM tropical SSTs were up to 5^{o}C cooler than CLIMAP in some regions (Guilderson et al., 1994; Lee and Slowey, 1999; Mix et al., 1999; Hostetler et al., 2006). Although disagreement still exists among several of the proxies (Crowley, 2000; Mix, 2006), consensus appears to be emerging that while SSTs over the entire tropics were on average only slightly cooler than CLIMAP, regional cooling and changes in the position and magnitude of the latitudinal gradient of SSTs may have produced atmospheric cooling found in terrestrial records (Pollard and Thompson, 1997; Hostetler and Mix, 1999; Crowley, 2000; Lea et al., 2000; Mix et al., 2001; Greene et al., 2002; Hostetler et al., 2006).

Because climatic inferences from tree-line records may be compromised by the effects of lower CO_2 at the LGM (Jolly and Haxeltine, 1997), former glaciers remain the principal source of information on high-altitude tropical paleoclimate. Glacial records are particularly important because they yield information about changes in high-elevation temperature, atmospheric water vapor and lapse rates (Broecker, 1997; Greene et al., 2002). In most cases, however, the age of maximum tropical glaciation and depression of the equilibrium line altitude (ELA) remain poorly constrained, complicating inferences of LGM climate (Rind and Peteet, 1985). Moreover, many tropical areas experienced large and abrupt climate changes within a few thousand years of the LGM (Thompson et al., 1995; Baker et al., 2001; Kienast et al., 2001, 2006) that were well within the uncertainties of presumed LGM moraine ages, and may have been deposited during millennial-scale events rather than during the LGM.

Well-preserved glacial deposits on Mauna Kea, Hawaii, (Fig. 1) are the only record of glaciation in the northern subtropical Pacific Ocean, and thus provide an important constraint on the magnitude and timing of ice-age climate change in this region. Recent work has improved the chronology of late-Pleistocene Mauna Kea glaciation (Blard et al., 2007; Pigati et al., 2008), but the small number of dates leaves large uncertainties. Here we report 42 new cosmogenic ^{3}He ages on glacial boulders and striated bedrock that significantly improve the chronology of the LLGM and deglacial history of the Mauna Kea ice cap, thus providing additional constraints on the potential controls of past climate change in the northern subtropical Pacific.

2. Physical setting

The island of Hawaii is located in the central subtropical North Pacific at 19.7º N¸ 155.5º W (Fig. 1). The topography of the island is dominated by the two large shield volcanoes: Mauna Kea (summit elevation of 4209 m) and Mauna Loa (summit elevation of 4169 m). A ~70 km^2

ice cap mantled the top of Mauna Kea during the last glaciation (Porter, 1979). Given its comparable elevation, Mauna Loa likely was also glaciated, but any evidence of Pleistocene glaciation has presumably been removed by Holocene volcanism (Porter, 2005).

The climate of Hawaii is dominated by the presence of the northeasterly (NE) trade winds that are more frequent in summer (80% – 95% of the time) than winter (50% – 80% of the time). The trade winds are associated with the Pacific High pressure cell situated east of the island and which tracks the seasonal position of the sun. Subsidence associated with the Pacific High maintains a temperature inversion that averages 2000 m in altitude. On Hawaii, the trade winds deliver substantial orographic precipitation below this inversion, but at higher altitudes, subsidence inhibits vertical atmospheric motion and thus development of clouds and precipitation. Precipitation that occurs on the summit of Mauna Kea is associated with weakening of the inversion by synoptic-scale weather systems that originate at higher latitudes (Blumenstock and Price, 1974).

3. Previous work

3.1 Stratigraphy and geochronology

Porter (1979) and Wolfe et al. (1997) mapped glacial deposits of three different ages on the summit of Mauna Kea and identified their relation to Pleistocene and Holocene lava flows. Subaerially exposed lavas on Mauna Kea form a cap that consists of basaltic lava overlain by hawaiitic lava and conceals the underlying main shield-forming basalts. The basaltic lava comprises the Hamakua Volcanics, which erupted between approximately 250 ka and 70-65 ka. The Hamakua Volcanics are further subdivided into the Hopukani Springs and Liloe Springs Volcanic Members, with ages of ~150-200 ka and 100-150 ka, respectively (Wolfe et al., 1997). These two members are separated by the Pohakuloa Glacial Member, which is poorly exposed with little known about its regional distribution (Porter, 1979). Younger deposits of the Waihu Glacial Member occur as a lens within, and as surficial deposits on top of, the Liloe Springs Volcanic Member. Moraines of the Waihu Glacial Member are subdued (Fig. 2), and most boulders lying at the surface are pitted or spalled (Porter, 1979). K/Ar dating of related volcanics are 100-150 ka, possibly as young as 70 ka (Wolfe et al., 1997), and one ^{36}Cl age on a glacial boulder is 68 ± 5 ka (Zreda et al., 1991).

The hawaiitic Laupahoehoe Volcanics were erupted between approximately 65 and 4 ka. Deposits of the final glaciation on Mauna Kea's summit, referred to as the Makanaka Glacial Member, are intercalated with the Laupahoehoe Volcanics. Porter (1979) distinguished two drifts associated with Makanaka glaciation. The older drift is characterized by subdued moraines that occur discontinuously around the summit region, and in places are buried by moraines of the younger drift or by lava flows. K/Ar ages suggest that this drift was deposited between 69 and 41 ka (Porter, 1979), whereas one ^{36}Cl age on a glacial boulder of 21.5 ± 0.2 ka (Zreda et al., 1991) suggests a significantly younger age. The younger drift of the Makanaka Glacial Member is characterized by prominent arcuate moraines on the southwest, north, and east sides of the mountain (Fig. 2). Radiocarbon ages suggest that the younger drift of the Makanaka Glacial Member was deposited sometime between 30 and 9 ka (Porter, 1979), while one ^{36}Cl age on a glacial boulder is 18.5 ± 0.2 ka (Zreda et al., 1991).

Wolfe et al. (1997) could not confirm Porter's hypothesis for an ice-free interval within the Makanaka glacial episode, but field relations suggest evidence for a fluctuating ice front. K/Ar ages on ice-contact lava flows suggest that the Makanaka glaciation was underway by about 40 ka, and deglaciation occurred approximately 13 ka (Wolfe et al., 1997). A ^{36}Cl age on striated bedrock from the summit of Mauna Kea of 14.4 ± 0.1 ka (Zreda et al., 1991) and a calibrated ^{14}C age of 14.7± 0.7 cal ka BP from basal sediments taken from Lake Waiau near the summit of Mauna Kea (Peng and King, 1992) supports this age for deglaciation.

Blard et al. (2007) used ^{3}He surface exposure dating to investigate the timing of glaciation in the Pohakuloa Gulch on the southwest flank of Mauna Kea (Fig. 1). They interpreted three ages from the LLGM moraine to indicate continuous occupation by LLGM ice between 19 ka and 16 ka. A suite of moraines inset from their older moraine yield, in stratigraphic order, ages of 14.6 ± 1.5 ka (N = 1), 16.5 ± 1.7 ka (N = 3), and 14.5 ± 1.5 ka (N = 1), which Blard et al. (2007) interpreted as evidence for a deglacial stillstand, with final deglaciation occurring ~15 ka.

Pigati et al. (2008) reported ^{36}Cl ages on boulders associated with the older Makanaka drift (N=3) and the younger Makanaka drift (2 sites, N=3 at each), suggesting ages of moraine abandonment of 23.1 ± 2.5 ka and 13.0 ± 0.8 ka, respectively. They also reported ^{36}Cl ages from a flood deposit that occurs distal to a Makanaka moraine (N=7), with a range from 10.7 ± 1.5 ka to 14.1 ± 1.2 ka.

3.2 Paleoclimate inferences from the Mauna Kea glacial record

Hostetler and Clark (2000) modeled a 63% increase in precipitation during the LGM which, combined with a 3.5^{o}C cooling, sustained a Mauna Kea ice cap of Makanaka extent. Blard et al. (2007) used a simplified ice flow and glacier mass balance model to constrain the range of possible temperature and precipitation conditions that would support such an ice cap. Based on an assumption of either no change in precipitation or reduced precipitation suggested from a low-altitude pollen record on Oahu (Hotchkiss and Juvik, 1999), they inferred a high-altitude cooling of 7 ^{o}C. Using the higher precipitation modeled by Hostetler and Clark (2000), however, reduced the required amount of cooling to 4.4 ± 0.9^{o}C, in agreement with Hostetler and Clark (2000).

To explain the apparent disagreement with the Oahu pollen record (Hotchkiss and Juvik, 1999), Hostetler and Clark (2000) suggested that a weakening of the subtropical high-pressure cells (STHs) during the LGM induced an increase in the mean altitude of the base of the tropical inversion, with attendant drier conditions at lower altitudes and wetter conditions at higher altitudes. These wetter conditions on the summit of Mauna Kea, combined with cooler subtropical Pacific SSTs (Lee and Slowey, 1999; Lee et al., 2001), supported the Mauna Kea ice cap during the LGM.

4. Sampling locales

The new cosmogenic ^{3}He dates were measured on peridotite and gabbro xenoliths found in hawaiite erratics derived from the Laupahoehoe Volcanics (Wolfe et al., 1997). These xenoliths are comprised of large mineral grains (up to 5 mm diameter) of olivine and clinopyroxene. The Laupahoehoe Volcanics, which are the primary parent material for Makanaka moraines, are no older than 107 ± 13 ka and are likely younger than ~70 ka (Wolfe et al., 1997). Many Laupahoehoe flows within the Makanaka glacial limit were erupted subglacially, or show ice-contact features around their flow perimeters (Porter, 1987). Xenolith-bearing erratics derived from this volcanic unit, however, only occur on the south flank of the volcano, thus limiting sample locations to this area.

We sampled relatively large (35-95 cm), subrounded to subangular boulders situated on low-angle (< 10°) moraine crests. Boulders were selected for xenolith presence, boulder size, the mineral content of xenoliths and the orientation of xenoliths when present in boulders. Wherever possible, samples were taken within 10 cm of the crest of a boulder and preferably on the boulder crest. The orientation of the xenoliths relative to various boulder faces was recorded in order to correct for self-shielding by the boulder. To correct for topographic shielding, we recorded the inclination and azimuth of major features on the horizon, although this correction proved to be minor (< 1%) for the open topography of the Mauna Kea summit area. Xenolith-bearing bedrock samples were taken with similar attention to geometry, potential shielding, orientation as well as lateral proximity to nearby surficial deposits. Some xenoliths displayed preferential, cavernous weathering that was limited to 1-2 cm for which a correction was applied. Preservation of striations and glacial polish on bedrock indicates that subglacial erosion occurred when ice was present, and that weathering and erosion since deglaciation has been minimal.

The sampling sites include four individual moraines, boulders from an alluvial fan, striated bedrock, and a single boulder near Lake Waiau within 200 m elevation of the summit (Fig. 2). Sample size was constrained by the presence of xenolith-bearing boulders on individual landforms. The most-sampled landform is the right lateral moraine of the Waikahalulu Gulch (N = 10). The other landforms, in descending order of sampling density, are a proximal moraine east of cone A (Cone A M2; N = 6), bedrock within Waikahalulu Gulch (N = 5), boulders on a flood deposit (N = 4), a moraine between Pohakuloa and Waikahalulu gulches (MBG; N = 3), a distal moraine east of cone A (Cone A M1; N = 2), and a single boulder adjacent to Lake Waiau.

Stratigraphically, the oldest sampled landforms are the MBG and the Cone A M1 moraines. The sampled right-lateral moraine of Waikahalulu Gulch cross-cuts the MBG moraine, indicating a readvance of ice down the gulch (Porter, 1979). There is only thin glacial drift up-slope from the Waikahalulu Gulch moraine suggesting that this moraine represents deposition during the last stillstand before final deglaciation. The only plausible Laupahoehoe Volcanic source material for the Waikahalulu Gulch moraine and the MBG moraine is the Puu Waiau flow, which has a single K/Ar age of 107 ± 13 ka (Wolfe et al., 1997).

The more distal position of the Cone A M1 moraine relative to the Cone A M2 moraine indicates its greater age. The source of hawaiite boulders on these two moraines was likely the Puu Wekiu flow, which forms the summit of Mauna Kea and has a lateral contact with the Puu Waiau flow. The Puu Wekiu lava has no numerical age control, but is stratigraphically younger than the Puu Poliahu flow, which has a single K/Ar age of 52 ± 15 ka, and older than the synglacially erupted Puu Hau Kea flow, with a single K/Ar age of 39 ± 7 ka. The Puu Wekiu flow also displays features associated with subglacial eruption (Porter, 1987; Wolfe et al., 1997). The relationship between the subglacially erupted Puu Wekiu flow and the ice-contact Puu Hau Kea flow suggests that ice associated with the Makanaka glaciation was present on Mauna Kea at some time between 32 ka and 67 ka.

We also sampled an alluvial fan that originates at a V-shaped gulley eroded through the Cone A M2 moraine, and is characterized by discrete, well-defined edges with the most distal deposits extending only a few hundred meters beyond the moraine. These characteristics of the fan are similar to those fans that formed from catastrophic drainage of moraine-dammed lakes (O'Connor et al., 2001), suggesting a one-time episode of deposition. Paleo-shorelines of the lake dammed by the Cone A M2 moraine occur on the eastern slopes of Cone A (Fig. 3).

The bedrock sample sites are upslope of the Waikahalulu Gulch moraine and are from outcrops of both the Puu Waiau and Puu Wekiu flows (Wolfe et al., 1997). Finally, the single sample from near Lake Waiau sits directly upon the Puu Hau Kea flow surface, and is likely derived from these lavas.

5. ^{3}He analysis and age reporting

Olivine and clinopyroxene crystals were separated from xenoliths by crushing and manual separation; nine xenoliths yielded both mineral phases which allowed a direct comparison of the results. The separated mineral phases were first crushed *in-vacuo*, which preferentially releases the inherited, magmatic ^{3}He and ^{4}He. The crushed minerals were then heated in a double-vacuum resistance furnace to release all remaining helium, which is a combination of inherited helium and cosmogenic helium. The mass spectrometry was carried out using a dedicated automated extraction line and mass spectrometer at Woods Hole Oceanographic Institution (WHOI), using well established techniques (e.g., Kurz, 1986; Kurz et al., 1990; Licciardi et al., 2006). The cosmogenic component is calculated using the inherited ratio $(^{3}He/^{4}He)_{i}$ from the crushing and the total amount of ^{4}He, $\Sigma^{4}He$. The cosmogenic helium component $^{3}He^{*}$, is calculated as:

$$^{3}He_{i} = \Sigma\, ^{4}He \left(\frac{^{3}He}{^{4}He}\right)_{crush} \tag{1}$$

$$^{3}He^{*} = \Sigma\, ^{3}He - {}^{3}He_{i} \tag{2}$$

The helium measurements from crushing and melting of the mineral separates, as well as the calculated ages, are reported in Table 1. The blanks during the course of the measurements were typically 2-4 x 10^{-11} cc He STP, requiring negligible corrections for the sample sizes analyzed (~ 0.3 grams). Air standards and procedural blanks were repeated before and after each sample, and the peak heights and accuracy of the isotopic compositions were verified with the WHOI glass standard (Kurz et al., 2005) and with bracketing air standards. Uncertainties in $^{3}He^{*}$ are computed from the quadrature sum of analytical uncertainties and are typically 1-3%.

Several recent studies have suggested the importance of grain-size dependent loss of cosmogenic ^{3}He during the vacuum crushing step (Yokochi et al., 2005; Blard et al., 2006). If the wide scatter in loss of cosmogenic ^{3}He discussed by Blard et al. (2006) were important, however, we would not expect the consistent ^{3}He production rates that have been calculated from a number of mid- and high-latitude sites using the techniques of Kurz (1986) (see also Goehring et al., 2010). In order to test this, we analyzed both whole grains and crushed powder for one of the samples (CK03-7). The results were identical for the whole grains and the powder, confirming that the WHOI crushing procedure yielded no loss of cosmogenic ^{3}He. The ^{3}He production rate scatter is most likely related to geological uncertainties and the systematic effects of changing geomagnetic field or air pressure. Note also that the crushed (magmatic) helium isotopic compositions are within the range observed for subaerial Mauna Kea (Kurz et al., 2004)

For the latitude of Hawaii (20°N), variations in geomagnetic intensity and in the strength and position of the geomagnetic dipole can cause some of the largest changes in effective production rates on earth (Kurz et al., 1990; Dunai, 2000; Gosse and Phillips, 2001). On Hawaii, Kurz et al. (1990) discussed the integrated effect of the strength of the magnetic dipole on ^{3}He production. There are now five widely used production rate scaling schemes for calculating exposure ages (Balco et al., 2008; Goehring *et al.*, 2010). Ages were calculated using all five production rate scaling schemes (Fig. S1) as described by Goehring *et al.* (2010). We report ages based on the Lifton et al. (2005) scheme because it includes a time-dependent scaling that incorporates the impact of changes in the magnetic field on the cosmic ray flux, which is particularly pronounced at high-altitude tropical sites. Other corrections include inclusion of the boulder geometry corrections reported by Masarik and Wieler (2003) as well as topographic shielding, which was small (< 1%). The combined topographic shielding and boulder shape corrections are denoted Σ_{corr} in Table 1. We have included a sample thickness correction using a density for the peridotite xenoliths of 3.3 g cm^{-3}. There is uncertainty in this correction in that the xenoliths reside in lower density basalt such that the effective self-shielding density is likely somewhat less than we've used.

The plotting convention used here displays the ages of all samples on each landform with error bars that combine the analytical uncertainty in measured $^{3}He^{*}$ concentrations and the uncertainty in the production rate and scaling. The calculated age of each landform is the boulder mean age excluding outliers; we interpret this age as the constraining the time of final moraine occupation (i.e., deglaciation). The error associated with the calculated age is the root sum of squares (RSS) of the standard error (calculated as $\sigma N^{-0.5}$, where σ is the standard deviation between ages and N is the number of samples) and the mean error for all boulders contributing to the mean age.

We identify outliers as follows. First, we exclude all ages that are <10 ka. Several of the <10 ka ages are from samples collected from boulder faces near the soil surface (CK03-4, CK03-8, AN06-19). Removal of other outliers is based on their falling outside the range of uncertainty calculated as above. This is shown graphically in figures showing the distribution of ages in that the uncertainty of excluded samples falls outside the uncertainty range calculated as above. Excluding such ages is further justified when viewing the summary probability plots (“camel plots”). The removed samples yield a Gaussian-like distribution indicating their origin from a single age distribution whereas multi-humped summed probabilities indicate multiple distributions. Otherwise, we include suspect ages lacking field or rigorous statistical justification for rejecting those ages. In most cases, including outliers does not alter the mean age but increases the uncertainty in that age.

6. Results

6.1 ^{3}He ages on olivine versus clinopyroxene

The nine ^{3}He ages for olivine and clinopyroxene pairs from the same xenolith, combined with two similar pairs of ages reported by Blard et al. (2007), are in good agreement (Fig. 4), supporting the use of either mineral phase for surface exposure dating at Mauna Kea. We average the two ages from each xenolith in reporting the age of the associated boulder. The remaining ages are derived from olivine (N = 7) or clinopyroxene (N = 18) mineral separates from each sample.

6.2 Age of initial deglaciation from the LLGM

The oldest ^{3}He ages are associated with the stratigraphically oldest moraines (MBG and Cone A M1) (Fig. 2, 5A). Although the MBG moraine is part of a recessional sequence, it is only 200 m horizontally upslope from the mapped extent of the LLGM (Porter, 1979), so deposition likely occurred shortly after retreat from the maximum extent. Therefore, we combine the boulder ages from these two moraines in calculating the age of retreat from the LLGM. We exclude one of the samples from the Cone A M1 moraine based on the criteria described above (AN06-05). The remaining four ages suggest that deglaciation from the LLGM occurred 22.2 ± 2.7 ka (Fig. 5A).

In reporting their ^{3}He ages, Blard et al. (2007) used a production rate of 128 ± 5 at g^{-1} yr^{-1} and scaling from Stone (2000) and Dunai (2000). If we follow our protocol of combining ages from a single landform and interpreting the mean age as the age of deglaciation, then their three ages from the LLGM moraine in Pohakuloa Gulch, just to the west of the MBG moraine, indicate that deglaciation began 18.3 ± 1.8 ka. When we recalculate their LLGM ages from Pohakuloa Gulch using the preferred production rate (118 ± 14 at g^{-1} yr^{-1}) (Licciardi et al., 1999,

2006) and the Lifton scaling, this age becomes 19.6 ± 2.4 ka, which is in agreement with our ages. We thus combine their ages with ours, which suggests that deglaciation from the LLGM occurred 20.5 ± 2.5 ka.

Based on three ^{36}Cl ages on boulders from older Makanaka drift on the opposite (north) side of Mauna Kea from where our samples are located, Pigati et al. (2008) derived an age of 23.1 ± 2.5 ka for deglaciation, in agreement with the new ^{3}He ages. Altogether, there are now 10 samples from boulders deposited during the LLGM, making this age determination robust.

6.3 Age of the final deglaciation

We calculate a mean age of 14.6 ± 1.9 ka for the Waikahalulu Gulch moraine (Fig. 5B), confirming the cross-cutting relationship that suggested that this moraine is younger than the MBG moraine (Porter, 1979). In calculating this age, we excluded two young ages (< 10 ka; CK03-08 and AN06-11). We also recalculated the five Blard et al. (2007) ^{3}He ages on three recessional moraines from Pohakuloa Gulch using the same production rate (118 ± 14 at g^{-1} yr^{-1}) and scaling, yielding a mean age of 15.9 ± 2.0 ka, which is within error of the new ^{3}He ages. The presence of several recessional moraines in Pohakuloa Gulch, and their absence upvalley from the Waikahalulu Gulch moraine, implies slightly different recessional behavior of this lobe of the ice cap, although the overlapping ages for these three landforms implies that deglaciation occurred rapidly.

Together with the calibrated radiocarbon age from Lake Waiau of 14.7 ± 0.7 cal ka BP as well as the single ^{3}He age of 15.7 ± 1.9 ka from this study, both of which are near the summit of Mauna Kea, this deglacial geochronology indicates rapid deglaciation of the Mauna Kea ice cap by ~15 ka. This age, however, is older than the deglaciation age suggested by ^{36}Cl dates reported by Pigati et al. (2008) (13.0 ± 0.8 ka) on samples of younger Makanaka drift from the northwest and west sides of Mauna Kea. In particular, although these ^{36}Cl ages overlap with the ^{3}He ages at 1 σ, they are significantly younger than the calibrated ^{14}C age from Lake Waiau. We thus conclude that the Pigati et al. (2008) age for younger Makanaka drift is too young, perhaps due to geological uncertainties associated with the small sample population (N=3 from 2 sites) or from differences in the systematics and scaling of the two nuclides.

6.4 Ice-cap fluctuation between the LLGM and final deglaciation

Of the five ^{3}He ages obtained on bedrock surfaces upslope from the Waikahalulu Gulch moraine, we excluded a young age of 10.8 ± 1.3 ka (AN06-19) on a surface that was within 50 cm of a deflating colluvial surface. The remaining four ages yield a mean age of 18.6 ± 2.5 ka (Fig. 5B), which is intermediate between our estimate of the initial deglaciation from the LLGM and the age of final deglaciation.

The presence of this intermediate age upslope from the younger Waikahalulu Gulch moraine (i.e., in a stratigraphically younger position) suggests inherited $^{3}He^{*}$ from previous exposure. Significant exposure prior to the LLGM is unlikely, however, because the bedrock samples are from two lava flows with differing eruption ages, which should thus have two different exposure histories, yielding different amounts of inherited $^{3}He^{*}$. Moreover, one of the lava flows erupted subglacially some time after ~67 ka (Wolfe et al., 1997). Although this age allows substantial time to accumulate $^{3}He^{*}$, the presence of subglacially and ice-contact erupted lava flows between this time and deposition of the LLGM moraines indicates that some duration of ice cover further reduced the time of bedrock exposure to cosmic rays.

When factoring in glacial erosion, a scenario of exposure prior to the LLGM and continuous ice cover between the LLGM and final deglaciation becomes an even less likely explanation for the bedrock ages. For example, if the site were continuously exposed from 67 ka to 20.5 ka and was then covered by ice from 20.5 ka to 14.6 ka (clearly a maximum exposure history given that the site was likely covered by ice prior to 20.5 ka), even a relatively slow glacial erosion rate of 0.3 mm yr^{-1} during this interval would reduce the amount of inherited $^3He^*$ to 7% of its pre-LLGM amount, leaving too little remaining $^3He^*$ to account for the observed bedrock age. Instead, ~60 kyr of exposure prior to the LLGM (i.e., starting at least 81 ka) is required to accumulate sufficient $^3He^*$ and account for the ~4 kyr worth of prior-exposure (the difference between the bedrock age of 18.6 ka and our final deglaciation age of 14.6 ka) remaining after erosion. Halving erosion rates would still require ~30 kyr.

Given that substantial pre-LLGM inheritance is an unlikely explanation for the age of the bedrock surface, its intermediate age instead suggests a fluctuation of the Mauna Kea ice-cap margin following the LLGM. Specifically, retreat of ice from the LLGM position to somewhere upslope of the dated bedrock surface simultaneously initiated exposure of the LLGM moraine and the bedrock surface. The bedrock surface subsequently remained exposed for some time prior to a readvance of the ice margin to the position marked by the Waikahalulu Gulch lateral and Pohakuloa Gulch recessional moraines. This readvance resulted in shielding by the overlying ice, and the polished and striated features of the bedrock surface indicate that some subglacial erosion occurred. Finally, deglaciation occurred at ~14.6 ka and the sampled bedrock surface has since been exposed.

We investigate various combinations of erosion rate and ice-cover duration required to explain the observed $^3He^*$ concentration. We first subtract the $^3He^*$ accumulated after deglaciation using the average production rate and the mean deglacial age of 14.6 ka. The remaining helium component ($[^3He^*]_r$) is then a product of production during the ice-free interval prior to readvance and the amount of material eroded during the readvance. For simplicity, we assume a single ice-margin fluctuation between the LLGM and deglaciation. The amount of helium that accumulated during this period is given as:

$$\left[{}^{3}He^{*}\right] = t_{noice} P^{*} \exp\left(\frac{-\rho\,\epsilon\left(5900 - t_{noice}\right)}{\Lambda}\right) \qquad (3)$$

Where t_{noice} is the total ice-free time, P^{*} is the mean scaled production rate for the bedrock surface, ρ is rock density (taken as 2.2 g cm^{-3} assuming basalt was the shielding material), ε is the erosion rate, 5900 years is the interval between the LLGM and final deglaciation, and Λ is the attenuation length for production of ^{3}He (165 g cm^{-2}; Kurz et al., 1990). We solve equation 3 for t_{noice} iteratively with erosion rates ranging from no erosion to 0.65 mm yr^{-1} (Fig. 6). We also calculate the duration of ice cover prior to the LLGM that would be required to reduce the amount of inherited $^{3}He^{*}$ to a value of 10% of the amount present prior to the advance culminating in the LLGM and thus resetting the $^{3}He^{*}$ clock. If as much as 20 kyr of exposure occurred prior to advance leading to the LLGM, a 10% value for inheritance is within the age uncertainty.

The results allow convergence on an appropriate erosion rate as well as an estimate of the duration of ice-free conditions between the LLGM and final deglaciation (Fig. 6). Assuming that the ice advance leading to the LLGM covered the bedrock sites for a plausible duration of 5 kyr to 10 kyr, then erosion rates of 0.2 mm yr^{-1} to 0.4 mm yr^{-1} are required to reduce inherited $^{3}He^{*}$ to <10% of the pre-LLGM amount. These erosion rates correspond to bedrock erosion rates for glaciers with a low mass flux (Hallet et al., 1996). Inserting this range of erosion rates into equation 3 yields a duration of ice-free conditions of 4.8 kyr to 5.4 kyr, suggesting that the readvance lasted from 0.5 kyr to 1.1 kyr. Adding these durations to our age of deglaciation (14.6 ka) implies that ice readvance began between 15.1 ka to 15.7 ka.

6.5 Age of the Cone A M2 moraine and the flood deposit

Of the six boulders sampled from the Cone A M2 moraine, ^{3}He ages on three boulders are in good agreement, with a mean age of 11.9 ± 1.5 ka, while three ^{3}He ages appear to be outliers (Fig. 5D). The ^{3}He ages from the flood deposit (Fig. 5E) include two that are equivalent to the Cone A M2 age and two that fall within the age population from the Waikahalulu Gulch moraine. Pigati et al. (2008) reported seven ^{36}Cl ages from this deposit that range from 10.7 ± 1.5 ka to 14.1 ± 1.2 ka, in good agreement with our two younger ^{3}He ages, and interpreted the deposit as having formed by meltwater from a retreating Makanaka ice cap over this 3.4-kyr time interval. We suggest, however, that such a long duration of deglaciation (3.4 kyr) is unlikely for this relatively low-volume ice cap. Moreover, the physical characteristics of the alluvial fan suggest deposition from a catastrophic flood (O'Connor et al., 2001) rather than a multi-millennial outwash deposit. Finally, we consider it highly unlikely that, after complete deglaciation no later than ~14.6 ka (as suggested by the ^{3}He ages and the calibrated ^{14}C age from Lake Waiau), the Mauna Kea ice cap subsequently rapidly reformed and advanced to a position that is nearly as extensive as the LLGM ice margin, particularly at this late time in the global deglaciation.

As discussed above, the characteristics of the alluvial fan are consistent with an origin by catastrophic drainage of a moraine-dammed lake (O'Connor et al., 2001). In this context, we interpret the age distribution from the Cone A M2 moraine and the flood deposit to indicate that at ~12 ka (corresponding in age to the Younger Dryas cold event), the moraine was breached by a lake dammed behind it (Fig. 3), with the downcutting of the outlet channel causing geomorphic instability of the moraine resulting in exposure of formerly buried boulders. The presence of a lake dammed behind the Cone A M2 moraine (Figure 3) indicates that the hydrologic regime at this time was wetter than today's arid climate. Finally, we note that ^{3}He ages on two boulders on the flood deposit are comparable in age to the Waikahalulu Gulch moraine, suggesting that the boulders may have been derived from the original Cone A M2 moraine surface at the time that the moraine was breached, and thus reflect true age of the moraine.

6.6. Influence of moraine degradation

In general, the ^{3}He ages on the MBG, Cone A M1, and Waikahalulu Gulch moraines provide a geochronological framework that is consistent with the stratigraphic relationships of the moraines. Nevertheless, younger outlier ^{3}He ages occur in each age population, suggesting morphologic changes to the moraines that resulted in post-depositional exposure of boulders. Blard et al. (2007) noted this tendency in their data, and although they attempted to reduce its impact by only accepting ages from boulders larger than 80 cm in height, their results still show considerable scatter.

Modeling studies of glacial landform morphology have shown that substantial reductions in crest height are possible on 10^{3}-yr time-scales, especially on matrix-supported moraines such as those on Mauna Kea (Hallet and Putkonen, 1994; Putkonen and Swanson, 2003; Ivy-Ochs et al., 2007). For moraines with equivalent present-day crest heights and ages, model results suggest that as much as 15 m of surface lowering may occur since deposition. Nevertheless, our results from one group of moraines are consistent with those of Blard et al. (2007) from another group of moraines, and the overall results are consistent with the ages of glacier and climate events elsewhere (discussed below), suggesting that the majority of the boulders record the original time of moraine formation.

One possible explanation is that moraine soil deflation does not influence larger boulders, allowing them to lower passively with the moraine surface and maintain a stable exposed surface. This process would leave a selection of boulders with a full exposure history interspersed among a selection of more recently exposed boulders.

7. Paleoclimate insights from ice dynamical modeling

Previous authors have used positive-degree-day models along with the known areal extent of the ice caps to calculate mass balance fields that would have sustained maximum ice-cap extent over the bare topography (Hostetler and Clark, 2000; Pigati et al., 2008). Blard et al. (2007) introduced simplified ice dynamics with a cellular automata model with a constant one-bar basal shear condition. Of these approaches, only that of Hostetler and Clark (2000) used temperature (T) and precipitation (P) derived from a general circulation model (GCM), thus avoiding the issue of having to independently constrain one variable (T or P) in order to estimate the other.

Here we evaluate the mass balance fields generated by this previous work by coupling them with an ice-dynamics model, which is comprised of a two-dimensional, vertically integrated formulation of mass conservation and Glen's flow law. Similar formulations have previously been used in complex terrain (Fastook, 1987; Plummer et al., 2001; Kessler et al., 2006). We tested ranges of inputs and resulting mass balances with varying ice-dynamics parameters (ice stiffness, presence or absence of sliding, etc.) and the results are robust within reasonable ranges of these parameters. The ice dynamics are driven by spatially distributed glacier mass balance fields as used by Pigati et al. (2008) or as functions of elevation as used by Hostetler and Clark (2000) and Blard et al. (2007). Mass balance is coupled with ice dynamics allowing for mass balance/elevation feedbacks as ice thickens. The model simulations were run for 3000 years to ensure that steady state was reached.

Our approach to calculating the surface mass balance relies on two assumptions. The first is that the equilibrium line altitude (ELA) as derived by Porter (1979, 2005), Blard et al. (2007),and Pigati et al. (2008) applies to both the LLGM and the subsequent readvance. This ELA corresponds to 3780 m on the present topography of Mauna Kea (i.e., not adjusted for subsidence of the volcano). The second assumption is that the ELA of glaciers in the tropics corresponds to the 0^{o}C isotherm within $\pm 1^{o}$C for the range of plausible accumulation rates for Mauna Kea. This assumption is based on field evidence from tropical glaciers (Ohmura et al., 1992; Shi, 2002) and is born out theoretically (Kaser, 2001). Using this latter assumption and the mean temperature structure of the troposphere as given by radiosonde measurements from Hilo, Hawaii, the paleo-ELA indicates a 4.5 ± 1^{o}C cooling for the LLGM relative to present. We further constrain the ice cap's mass balance by calculating a mass balance gradient below the ELA that is a function of temperature lapse rate (Γ), number of melting days per year found in the outer tropics (t_{melt}), and degree day melt factor (DDF):

$$\frac{db}{dz} = \Gamma\, t_{melt}\, DDF \qquad (4)$$

We allow for a range of balance gradients to accommodate the likely range in these three parameters (5.4 – 6.6 ºC km^{-1} for Γ; 180 to 260 days for t_{melt}; and 6 to 8 mm ºC dy^{-1}). These constraints allow us to evaluate the precipitation enhancement that was required to sustain the Mauna Kea ice cap at these two times. Above the ELA, the balance gradient is determined by the maximum accumulation at the summit and the difference in elevation between the ELA and the summit.

To arrive at the optimal mass balance for glaciation of Mauna Kea, we explore a range of precipitation enhancement at the summit from 0.5 times present through 3 times present. The ablation gradient is allowed to vary, thus accommodating changes in temperature lapse rate, seasonality (seasonality controls the number of days in which melting can occur), and degree day melt factor. Finally, we allow for relatively small variations (±150 m in 75 m increments) about the presumed ELA of 3780 m which, allowing for the high lapse rate derived by Blard et al. (2007), corresponds to as much as a ±1^{o}C temperature variation at the ELA.

To determine which models most closely match the dated ice-cap extents, we develop a metric (cost function) based on a Gaussian filter of the location of the moraine crest. The Gaussian filtered moraine location will have the highest value at the moraine crest with tapering values up and down slope from the moraine. The filter was set to zero closest to the crest and decreasing to more negative values down slope (Fig. S2). Scores are summed wherever ice is present and the cost surface only applies to the vicinity of the S-SW flank of Mauna Kea where the dated moraines occur. Based on this construct, the cost surface allows models to accumulate more points as ice approaches the moraine crest; for ice that overruns the crest, points are subtracted. This provides an objective determination of the best-fitting reconstructed ice coverage (Fig. S2).

The results of the simulations for the SW portion of ice cap are given in Fig. 7 and 8, and the results for the entire ice cap are shown in Fig. S3 and S4. Overall, the mass balance fields derived from previous work do not result in growth of an ice cap of the size present at the LLGM nor the readvance phase. The simulations driven by mass balance gradients from Blard et al. (2007) (Fig. 7A) and Hostetler and Clark (2000) (Fig. 7B) yield the smallest LLGM ice caps. The Blard et al. (2007) reconstruction was based on drier and substantially colder-than-present

($7^{o}C$) conditions, while Hostetler and Clark (2000) reconstructed mass balance based on GCM simulations that showed conditions that were 63% wetter and moderately cooler ($3.5^{o}C$) than present. The mass balance estimate of Pigati et al. (2008) comes closest to generating the LLGM ice cap but it is too small overall (Fig. 7C).

Based on results from this optimization (Fig. S3), the best fit of the simulated LLGM ice cap to the mapped LLGM extent is obtained using a precipitation enhancement factor of 3 (Fig. 7D). Although the simulated LLGM ice cap overrides sample sites of the Cone A M1 moraine, its margin reaches the moraines of the Pohakuloa and Waikahalulu gulches (Fig. 7D) as well as the prominent lateral moraines on the north side of the volcano (Fig. S3D). The simulation also shows reasonably good agreement with the drift limit mapped elsewhere on the volcano (Fig. S3D).

Given that the post-LLGM readvance nearly reached the same extent as the LLGM extent, we obtain similar results for this event as for the LLGM event. The reconstruction from the mass balance estimate of Blard et al. (2007) only reaches the stratigraphically youngest Pohakuloa Gulch moraine, several hundred meters upslope from their lowest elevation readvance samples, whereas neither the similar-aged Waikahalulu Gulch moraine nor the Cone A M2 moraine is reached (Fig. 8A). Most importantly, the simulated margin remains far upslope of our dated bedrock samples that were overridden by this readvance. On the other hand, the mass balance estimate of Pigati et al. (2008) for their younger event (not interpreted as a readvance) generates an ice cap that covers the sites of our bedrock samples, nearly reaches the Cone A M2 moraine, and remains upslope of the Waikahalulu samples (Fig. 8B). Therefore, the cost analysis indicates that the best-fit of the simulated ice cap to the dated moraines is obtained again by increasing precipitation by 1.5 to 3 times the present amounts (Fig. 8C). The asymmetry in ice extent discussed by Porter (2005) is not addressed in this modeling due to the simplicity of the simulated mass balance (apparent in figure S2). The climate mechanism (discussed below) that is hypothesized to have enabled ice to grow on Mauna Kea calls for a reduction in trade wind strength, which was cited by Porter (2005) as the primary mechanism for generating the asymmetry. Alternatives such as wind loading from stronger west and northwest winds could also have cause enhanced accumulation and greater ice extent on the southeast sector of the volcano and scouring and reduced accumulation on the northeast flank. Lacking a proper wind distribution model, this is purely speculative.

8. Discussion

Blard et al. (2007) interpreted the spread in their three ^{3}He ages on the LLGM moraine as indicating that the LLGM occurred between 19 ka and 16 ka, whereas we interpret the mean of these ages as recording the time of final occupation of the moraine, with differences among the ages reflecting geological uncertainties. Including the three ^{3}He ages from Blard et al. (2007) with the new ^{3}He ages suggests that the Mauna Kea ice cap was at its LLGM extent until 20.5 ± 2.5 ka, which is significantly older than the Blard et al. (2007) interpretation. (Because terrestrial cosmogenic nuclide ages from a moraine do not record onset or duration of a glacial event, we do not know when the LLGM began.) In contrast, our ^{3}He ages for deglaciation from the LLGM position are younger than the ^{36}Cl ages for deglaciation reported by Pigati et al. (2008) (23.1 ± 2.5 ka), although given the small number of samples (N=3), this age difference may reflect larger geological uncertainties in their data set or larger uncertainties in the ^{36}Cl production rate (Gosse and Phillips, 2001). On the other hand, the new ^{3}He ages for LLGM deglaciation are in agreement with ^{10}Be ages of initial deglaciation elsewhere in the tropics and subtropics, which for the Lifton scaling is 18.9 ± 2.3 ka (Clark et al., 2009).

We attribute most of the high-altitude 4.5 ± 1^{o}C cooling to planetary cooling during the LGM. The local sea surface temperature cooling of ~3^{o}C (Lee et al., 2001) indicates that only moderate changes in lapse rate occurred during the LLGM. The enhanced precipitation is consistent with a southeastward shift in the Pacific High, decreased trade wind strength, and a southeastward shift in the storm track which would have increased both winter and summer precipitation over Hawaii, as simulated in GCMs (Yanase and Abe-Ouchi, 2007; Laine et al., 2009). The present-day occurrence of snow on the summit of Mauna Kea is associated with extratropical frontal cyclonic storms during winter (Blumenstock and Price, 1974), suggesting that such storms may have been more frequent during the LGM. Additional precipitation enhancement may have been associated with a weakening of the subtropical high-pressure cells during the LGM that caused an increase in the mean altitude of the base of the tropical inversion (Hostetler and Clark, 2000). Although a precipitation enhancement of three times present is large, the resulting precipitation amounts are still relatively dry at roughly 1.5 m at the summit of Mauna Kea.

Our results differ from previous work in identifying evidence for a significant fluctuation of the ice margin during the last deglaciation. Blard et al. (2007) interpreted their ^{3}He ages to suggest that the ice margin remained at its LLGM position until ~16 ka, retreated ~1 km and stabilized until ~15 ka (or during the interval we have identified as a readvance), and then rapidly deglaciated. Our inferred age for final Mauna Kea deglaciation is older than the mean of the ^{36}Cl ages reported by Pigati et al. (2008) (13 ka), particularly when accounting for the calibrated ^{14}C age from Lake Waiau. The Blard et al. (2007) and Pigati et al. (2008) results, however, can be reconciled with ours by interpreting their deglacial stillstand to instead correspond to the readvance represented by the Waikahalulu Gulch moraine, albeit with the ^{36}Cl ages being too young possibly due to geological uncertainties. Evidence for an ice-margin fluctuation is provided by the age of our bedrock samples and is consistent with the Makanaka ice cap's capability for rapid climate response due to its small size.

The inferred Mauna Kea deglacial history disagrees with the monotonic deglacial warming observed in some tropical and subtropical SST records beginning ~19 ka (Lea et al., 2000; Visser et al., 2003; Martinez et al., 2003; Kiefer and Kienast, 2005). Instead, our results suggest a deglacial climate signal that is similar to the deglacial climate of the North Atlantic region, with ice-cap advance occurring during North Atlantic cold intervals and ice-cap retreat occurring during North Atlantic warm intervals. In particular, we note that the timing of the deglacial ice-cap readvance on Mauna Kea corresponds to a large reduction of the Atlantic meridional overturning circulation (AMOC) following H1, whereas the rapid deglaciation corresponds to the onset of the Bølling warm interval (Fig. 9A, 9B). However, we stress that our interpretations regarding the timing of these events is subject to the relatively large uncertainty associated with the dating technique at high altitude in the tropics, which has been the case with previous cosmogenic nuclide dating studies on Hawaii. We thus consider our interpretation of glacial events on Hawaii and their relation to millennial-scale climate change as a working hypothesis that requires further testing through improved understanding of ^{3}He production rates during this interval.

Given the similarity in the timing of North Atlantic climate change during the last deglaciation (and associated caveats), we propose that the temperature and precipitation changes in the subtropical Pacific that caused the ice-cap fluctuation reflect atmospheric responses caused by changes in the strength of the AMOC. In particular, recent model simulations indicate that these atmospheric responses to an AMOC decrease may have been associated with a southward shift of the Intertropical Convergence Zone (ITCZ) in the Pacific basin and elsewhere. There is now widespread proxy evidence throughout the tropics and subtropics for such a shift of the ITCZ at the same time as the Mauna Kea ice-cap fluctuation (~16-14.5 ka) (Fig. 9). During this time, records show reduced Asian and Arabian Sea summer monsoons (Schulz et al., 1998; Wang et al., 2001; Ivanochko et al., 2005) (Fig. 9C-E), increased winds in southern East Africa (Johnson et al., 2002) (Fig. 9F), and drier and colder conditions in the Sulu and South China Seas (Rosenthal et al., 2003; Kienast et al., 2006) (Fig. 9G, 9H). Records from low-latitude sites near the Americas indicate drying of the tropical North Atlantic (Peterson et al., 2000) (Fig. 9I), drier and colder conditions in the East Pacific Warm Pool (Benway et al., 2006) (Fig. 9J), colder and wetter conditions off the Pacific coast of Columbia (Pahnke et al., 2007) (Fig. 9K), cooling in the eastern tropical Pacific (Kienast et al., 2006) (Fig. 9L), and wetter conditions in Bolivia (20^{o}S) (Baker et al., 2001) (Fig. 9M).

Results from a coupled atmosphere-ocean general circulation model (AOGCM) demonstrate one mechanism by which this shift in the ITCZ occurred in response to a large reduction in the AMOC (Zhang and Delworth, 2005). Specifically, these results show a southward shift in the Atlantic-basin ITCZ associated with a meridionally asymmetric tropical SST pattern about the equatorial Atlantic established by the AMOC decrease. The strong cooling in the tropical Atlantic enhances sea-level pressure in the eastern tropical Pacific, which weakens the climatological Hadley circulation there and causes anomalous southward surface winds across the equator in the eastern Pacific. This southward wind anomaly induces anomalous ocean upwelling and thus cooling in the eastern tropical Pacific north of the equator, and anomalous ocean downwelling and thus warming in the cold tongue south of the equator. The SST dipole anomaly across the eastern tropical Pacific further amplifies these responses, causing a southward shift in the ITCZ accompanied by a southwardly displaced Hadley cell. Because the Pacific High is a manifestation of the northern extent of the Hadley circulation over the Pacific, a southward shift in the Hadley circulation corresponds with a southward displacement of the Pacific High. These results are supported by a suite of AO-GCM simulations that similarly investigated the response of the Pacific to a weakening of the AMOC (Timmerman et al., 2007). In particular, these show positive zonal surface wind anomalies near Hawaii and northward in many of their simulations. As for the LGM, we thus suggest that the southward displacement of the Pacific High may have caused a greater frequency of cyclonic storms that provided increased moisture to the summit of Mauna Kea.

Another robust model response to a large reduction of the AMOC is the cooling of the extratropical North Pacific from the advection of cold Siberian air, especially in winter (Mikolajewicz et al., 1997; Vellinga and Wood, 2002; Zhang and Delworth, 2005). Cooling is particularly pronounced in the NW Pacific reflecting the growth of sea ice in that area (Vellinga and Wood, 2002). While the cooling was sufficient to cause a southward shift of the ITCZ, Chiang and Bitz (2005) found that the introduction of sea ice in the NW Pacific also caused a southward shift ITCZ. The mechanism behind this shift involves a progressive migration of cooler SSTs into the northern subtropical and tropical Pacific, with the ITCZ shift occurring when the SST anomalies reach the ITCZ latitudes. In any event, this result indicates that not only would the ITCZ shift be associated with a southward shift in the Pacific High, and thus increase the frequency of moisture-bearing extratropical cyclones reaching Hawaii, but would also cause SSTs around Hawaii to cool.

We note that the timing of final deglaciation on Mauna Kea (14.6 ± 1.9 ka) is in good agreement with the resumption of the AMOC that caused the onset of the Bølling warm interval, further supporting our hypothesis that changes in the AMOC strongly influenced the climate of Hawaii.

The final event dated on Mauna Kea is associated with rapid drainage of a lake dammed behind the Cone A M2. Although the drainage itself likely just represents breaching of the moraine by the lake, and is thus nonclimatic, the presence of the lake itself indicates wetter conditions than today. The dating of this event at ~12 ka is uncertain due to the small number of ^{3}He ages (and the scatter), but corresponds to the Younger Dryas cold interval, which is also related to a reduction of the AMOC (Fig. 9) (McManus et al., 2004). Accordingly, the evidence for wetter conditions at this time is consistent with our argument for wetter conditions on Hawaii during H1, also caused by a reduction in the AMOC.

9. Conclusions

The new ^{3}He ages suggest that the Mauna Kea LLGM ended 20.5 ± 2.5 ka, roughly coincident with the termination of the LGM elsewhere in the subtropics and tropics (Clark et al., 2009). We infer deglaciation from this maximum extent causing the terminus to retreat >3 km, followed by a readvance at 15.7 ka to 15.1 ka corresponding to the timing of a large reduction of the AMOC in the North Atlantic. Deglaciation was underway by 14.6 ± 1.9 ka and complete shortly thereafter, which corresponds to the resumption of the AMOC and the onset of the Bølling warm interval.

To explain the close relationship between the Mauna Kea deglacial chronology and that of climate changes originating in the North Atlantic, we point to a mechanism associated with changes in the transient position of the ITCZ. Climate on Hawaii is closely related to the position and strength of the Pacific High, which is a manifestation of the subsiding limb of the Hadley cell. Both modeling and proxy evidence for changes in the position and strength of the

Hadley cell agree with our deglacial history. Such a reorganization in atmospheric circulation is supported by our ice dynamics model and inferred climate scenario, which uniformly requires more precipitation than present day for glaciation to reach the observed extents on Mauna Kea. These results make it unlikely that LLGM and Heinrich glaciations were caused by drier-than-present conditions and the cooling of 6.5 to 7 ^{o}C suggested by Blard et al. (2007). The results presented here require more moderate cooling of 4.5 ± 1.0 ^{o}C and a precipitation enhancement of 3 times the modern precipitation rate at the summit. Such a precipitation increase could be supported by increased frequency of midlatitude frontal systems.

Acknowledgments. We thank Jorie Clark for help with sampling and Josh Curtice for his expertise in the laboratory. We also gratefully acknowledge the advice of Frank Trusdell and Dave Sherrod in the field, and the support provided by the entire University of Hawaii staff at the Mauna Kea support facility. Supported by the NSF Paleoclimate Program.

References

Baker, P., *et al*., 2001. Tropical climate changes at millennial and orbital timescales on the Bolivian Altiplano. Nature 409, 698-701.

Balco, G., Stone, J.O., Lifton, N.A., and Dunai, T.J., 2008. A complete and easily accessible means of calculating surface exposure ages or erosion rates from ^{10}Be and ^{26}Al measurements. Quat. Geochron. 3, 174-195.

Benway, H.M., Mix, A.C., Haley, B.A., and Klinkhammer, G.P., 2006. Eastern Pacific warm pool paleosalinity and climate variability: 0-30 kyr. Paleocean. 21, doi:10.1029/2005PA001208.

Betts, A.K., and Ridgeway, W., 1992, Tropical boundary layer equilibrium in the last ice age: Jour. Geophys. Res. 97, 2529-2534.

Blard, P.-H., R. Pik, J. Lavé, D. Bourlès, P.G. Burnard, R. Yokochi, B. Marty, and F. Trusdell, 2006. Cosmogenic ^{3}He production rates revisited from evidences of grain size dependent release of matrix-sited helium. Earth Planet. Sci. Let. 247, 222-234.

Blard, P.-H., J. Lavé, R. Pik, P. Wagnon, and D. Bourlès, 2007. Persistence of full glacial conditions in the central Pacific until 15,000 years ago. Nature 449, 591-596.

Blumenstock, D.I., and S. Price, 1974. The climate of Hawaii. *The Climates of States*, National Oceanic and Atmospheric Administration, 24 pp.

Bond, G.C., Showers, W., Elliot, M., Evans, M., Lotti, R., Hajdas, I., Bonani, G., Johnsen, S., 1999, The North Atlantic's 1–2 kyr climate rhythm: relation to Heinrich events, Dansgaard/Oeschger cycles and the little ice age. In: Clark, P.U., Webb, R.S., and Keigwin, L.D., eds., Mechanisms of global climate change at millennial time scales. AGU Geophys Monogr 112: 35–58.

Broccoli, A.J., 2000. Tropical cooling at the last glacial maximum: An atmosphere-mixed ocean model simulation. Jour. Climate 13, 951-976.

Broecker, W., 1997. Mountain glaciers: Recorders of atmospheric water vapor content? Global Biogeochem. Cycles 11, 589-597.

Chiang, J.C.H., and Bitz, C.M., 2005, Influence of high latitude ice cover on the marine Intertropical Convergence Zone. Clim. Dyn. 25, 477-496.

Clark, P.U., Dyke, A.S., Shakun, J.D., Carlson, A.E., Clark, J., Wohlfarth, B., Mitrovica, J.X., Hostetler, S.W., and McCabe, A.M., 2009, The Last Glacial Maximum: Science 325, 710-714.

CLIMAP Project Members, 1976, The surface of the ice-age Earth: Science 191, 1131-1137.

CLIMAP Members, 1981, Seasonal reconstructions of the Earth's surface at the last glacial maximum: Geol. Soc. Amer. Map & Chart Series MC-3.

Crowley, T.J., 2000, CLIMAP SSTs revisited: Clim. Dyn., 16, 241-255.

Dunai, T.J., 2000. Scaling factors for production rates of in situ produced cosmogenic nuclides: a critical reevaluation. Earth Planet. Sci. Let. 176, 157-169.

Goehring, B.M., M.D. Kurz, G. Balco, J.M. Schaefer, J. Licciardi, and N. Lifton, 2010. A reevaluation of *in situ* cosmogenic ^{3}He production rates. Quat. Geochron., doi:10.1012/j.quageo.2010.03.001.

Gosse, J.C. and F.M. Phillips, 2001. Terrestrial in situ cosmogenic nuclides: theory and application. Quat. Science Rev. 20, 1475-1560.

Greene, A.M., Seager, R., and Broecker, W.S., 2002, Tropical snowline depression at the Last Glacial Maximum: Comparison with proxy records using a single-cell tropical climate model: J. Geophys. Res., 10.1029/2001JD000670.

Guilderson, T., Fairbanks, R., and Rubenstone, J., 1994, Tropical temperature variations since 20,000 years ago: modulating interhemispheric climate change: Science 263, 663-665.

Hallet, B. and J. Putkonen, 1994. Surface Dating of Dynamic Landforms: Young Boulders on Aging Moraines. Science 265, 937-940.

Hallet, B. L. Hunter, and J. Bogen, 1996. Rates of erosion and sediment evacuation by glaciers: A review of field data and their implications. Global Planet. Change 12, 213-235.

Hostetler, S.W., and Mix, A.C., 1999, Reassessment of ice-age cooling of the tropical ocean and atmosphere: Nature 399, 673-676.

Hostetler, S.W. and P.U. Clark, 2000. Tropical climates at the last glacial maximum inferred from glacier mass-balance modeling. Science 290, 1747-1750.

Hostetler, S.W., N. Pisias, and A. Mix, 2006. Sensitivity of Last Glacial Maximum climate to uncertainties in tropical and subtropical ocean temperatures. Quat. Sci. Rev. 25, 1168-1185.

Hotchkiss, S. and J.O. Juvik, 1999. A Late-Quaternary Pollen Record from Ka’au Crater, O’ahu, Hawai’i. Quat. Res. 52, 115-128.

Ivanochko, T., Ganeshram, R.S., Brummer, G.-J. A., Ganssen, G., Jung, S.J.A., Moreton, S.G., and Kroon, D., 2005, Variations in tropical convection as an amplifier of global climate change at the millennial scale. Earth Planet. Sci. Let. 235, 302-314.

Ivy-Ochs, S., H. Kerschner, and C. Schlüchter, 2007. Cosmogenic nuclides and the dating of Lateglacial and Early Holocene glacier variations: The Alpine perspective. Quat. Int. 164-165, 53-56.

Johnson, T.C., Brown, E.T., McManus, J., Barry, S., Barker, P., and Gasse, F., 2002. A high-resolution paleoclimate record spanning the past 25,000 years in southern East Africa. Science 296, 113-116.

Jolly, D., and Haxeltine, A., 1997, Effect of low glacial atmospheric CO_2 on tropical African montane vegetation. Science 276, 786.

Kaser, G. 2001. Glacier-climate interaction at low latitudes. Jour. Glaciol. 47, 195-204.

Kessler, R.A., Anderson, R.S., and Stock, G.M., 2006. Modeling topographic and climatic control of east-west asymmetry in Sierra Nevada glacier length during the Last Glacial Maximum. Jour. Geophys. Res. 111, F02002, doi:10.1029/2005JF000365

Kiefer, T., and Kienast, M., 2005 Patterns of deglacial warming in the Pacific Ocean: a review with emphasis on the time intervalof Heinrich event 1. Quat. Sci. Rev. 24, 1063–1081.

Kienast, M., Steinke, S., Stattegger, K., and Calvert, S.E., 2001, Synchronous tropical South China Sea SST change and Greenland warming during deglaciation: Science 291, 2132-2134.

Kienast, M., S.S. Kienast, S.E. Calvert, T.I. Eglinton, G. Mollenhauer, R. François, and A.C. Mix, 2006. Eastern Pacific cooling during the last deglaciation. Nature 443, 846-849.

Kurz, M.D., 1986. *In situ* production of terrestrial cosmogenic helium and some applications to geochronology. Geochim. Cosmochim. Acta 50, 2855-2862.

Kurz, M.D., D. Colodner, T.W. Trull, R.B. Moore, and K. O'Brien, 1990. Cosmic ray exposure dating with in situ produced cosmogenic ^{3}He: results from young Hawaiian lava flows. Earth Planet. Sci. Let. 97, 177-189.

Kurz, M.D., J. Curtice, D.E. Lott, and A. Solow (2004). Rapid helium isotopic variability in Mauna Kea shield lavas from the Hawaiian Scientific Drilling Project. Geochem. Geophysics. Geosystems (G-cubed), AGU. 5, Q04G14, doi:10.1029/2002GC000439.

Kurz, M.D., M. Moreira, J. Curtice, D.E. Lott, J.J. Mahoney, and J.M. Sinton (2005) Correlated helium, neon and melt production on the super-fast spreading East Pacific Rise near 17 S. Earth and Planetary Science Letters 125-142.

Laine, A., et al., 2009, Northern Hemisphere storm tracks during the last glacial maximum in the PMIP2 ocean-atmosphere coupled models: energetic study, seasonal cycle, precipitation. Clim. Dyn. 32, 593-614.

Lea, D.W., D.K. Pak, and H.J. Spero, 2000. Climate impact of late Quaternary equatorial Pacific sea surface temperature. Science 289, 1719-1724.

Lee, K. E., N.C. Slowey, and T.D. Herbert. 2001. Glacial sea surface temperatures in the subtropical North Pacific: A comparison of $U^{k'}_{37}$, $d^{18}O$, and foraminiferal assemblage temperature estimates. Paleocean. 16, 268-279.

Lee, K.E. and N.C. Slowey, 1999. Cool surface waters of the subtropical North Pacific Ocean during the last glacial. Nature 397, 812-814.

Licciardi, J.M., Kurz, M.D., Clark, P.U., Brook, E.J., 1999. Calibration of cosmogenic ^{3}He production rates from Holocene lava flows in Oregon, USA, and effects of the Earth's magnetic field. Earth Planet. Sci. Let. 172, 261-271.

Licciardi, J.M., M.D. Kurz, and J.M. Curtice, 2006. Cosmogenic ^{3}He production rates from Holocene lava flows in Iceland. Earth Planet. Sci. Let. 246, 251-264.

Lifton, N.A., J.W. Bieber, J.M. Clem, M.L. Duldig, P. Evenson, J.E. Humble, and R. Pyle, 2005. Addressing solar modulation and long-term uncertainties in scaling in situ cosmogenic nuclide production rates. Earth Planet. Sci. Let. 239**.** 140-161.

Martinez, I., Keigwin, L., Barrows, T.T., Yokoyama, Y., and Southon, J., 2003. La Nina-like conditions in the eastern equatorial Pacific and a stronger Choco jet in the northern Andes during the last glaciation. Paleocean. 18, doi:10.1029/2002PA000877.

Masarik, J., ans R. Wieler, 2003. Production rates of cosmogenic nuclides in boulders. Earth Planet. Sci. Let. 216. 201-208.

McManus, J. F., Francois, R., Gherardi, J.-M., Keigwin, L.D., and Brown-Leger, S., 2004, Collapse and rapid resumption of the Atlantic meridional circulation linked to deglacial climate changes. Nature 428, 834–837.

Mikolajewicz, U., Crowley, T.J., Schiller, A., Voss, R., 1997. Modelling teleconnections between the North Atlantic and North Pacific during the Younger Dryas. Nature 387, 384–387.

Mix, A.C., 2006, Running hot and cold in the eastern equatorial Pacific. Quat. Sci. Rev. 25, 1147-1149.

Mix, A.C., Bard, E., and Schneider, R., 2001, Environmental processes of the ice age: land, oceans, glaciers (EPILOG): Quat. Sci. Rev. 20, 627-658.

Mix, A. C. *et al.*, 1999, Foraminiferal faunal estimates of paleotemperature: circumventing the no-analog problem yields cool ice age tropics: Paleocean. 14, 350-359.

O'Connor, J. E., Hardison, J. H. I., and Costa, J. E., 2001. Debris flows from failure of Neoglacial age moraine dams in the Three Sisters and Mount Jefferson Wilderness Area, Oregon. U.S. Geological Survey Professional Paper 1606, 93 p.

Ohmura, A., P. Kasser, and M. Funk. 1992. Climate at the equilibrium line of glaciers. Jour. Glaciol. 38, 397-411.

Pahnke, K., Sachs, J.P., Keigwin, L., Timmermann, A., and Xie, S.-P., 2007. Eastern tropical Pacific hydrologic changes during the past 27,000 years from D/H ratios in alkenones. Paleocean. 22, doi:10.1029/2007PA001468.

Peng, L. and J.W. King, 1992. A late Quaternary geomagnetic secular variation record from Lake Waiau, Hawaii, and the question of the Pacific nondipole low. Jour. Geophys. Res. 97, 4407-4424.

Peterson, L.C., G.H. Haug, K.A. Hughen, and U. Rohl, 2000. Rapid changes in the hydrologic cycle of the tropical Atlantic during the last glacial. Science 290, 1947-1951.

Pigati, J.S., Zreda, M., Zweck, C., Almasi, P.F., Elmore, D., and Sharp, W.D., 2008. Ages and inferred causes of late Pleistocene glaciations on Mauna Kea, Hawaii. Jour. Quat. Sci. 23, 683-702.

Pinot, S., G. Ramstein, S.P. Harrison, I.C. Prentice, J. Guiot, M. Stute, and S. Joussaume, 1999. Tropical paleoclimates at the Last Glacial Maximum: comparison of Paleoclimate Modeling Intercomparison Project (PMIP) simulations and paleodata. Clim. Dyn. 15, 857-874.

Pollard, D., and Thompson, S.L., 1997, Climate and ice-sheet mass balance at the last glacial maximum from the GENESIS version 2 global climate model: Quat. Sci. Rev. 16, 841-863.

Porter, S.C., 1979. Hawaiian glacial ages. Quat. Res. 12, 161-187.

Porter, S.C., 1987. Pleistocene subglacial eruptions on Mauna Kea. In Decker, R.W., T.L. Wright, and P.H. Stauffer eds. Volcanism in Hawaii: U.S. Geological Survey Professional Paper 1350, **1**, 587-598.

Porter, S.C., 2005. Pleistocene snowlines and glaciation of the Hawaiian Islands. Quat. Int. 138-139, 118-128.

Putkonen, J. and T. Swanson, 2003. Accuracy of cosmogenic ages for moraines. Quat. Res. 59, 255-261.

Rind, D. and D. Peteet, 1985. Terrestrial condition at the Last Glacial Maximum and CLIMAP sea-surface temperature estimates: Are they consistent? Quat. Res. 24, 1-22.

Rosenthal, Y., Oppo, D.W., and Linsley, B.K., 2003, The amplitude and phasing of climate change during the last deglaciation in the Sulu Sea, western equatorial Pacific. Geophys. Res. Let. 30, doi:10.1029/2002GL016612.

Schulz, H., von Rad U., Erlenkeuser, H., 1998, Correlation between Arabian Sea and Greenland climate oscillations of the past 110,000 years. Nature 393, 54–57.

Shi, Y., 2002. Characteristics of late Quaternary monsoonal glaciation on the Tibetan Plateau and in East Asia. Quat. Int. 97-98, 79-91.

Stone, J.O., 2000, Air pressure and cosmogenic isotope production: Jour. Geophys. Res. 105, 23753-23759.

Thompson, L.G. *et al*., 1995, Late glacial stage and Holocene tropical ice core records from Huascaran, Peru: Science 269, 46-50.

Timmerman, A., et al., 2007. The influence of a weakening of the Atlantic meridional overturning circulation on ENSO. Jour. Clim. 20, 4899-4919.

Vellinga, M., and Wood, R.A., 2002. Global climatic impacts of a collapse of the Atlantic thermohaline circulation. Clim. Change 54, 251-267.

Visser, K., Thunell, R., Stott, L., 2003, Magnitude and timing of temperature change in the Indo-Pacific warm pool during deglaciation. Nature 421, 152-155.

Wang, Y.J., H. Cheng, R.L. Edwards, Z.S. An, J.Y. Wu, C.-C. Shen, and J.A. Dorale, 2001. A high-resolution absolute-dated Late Pleistocene monsoon record from Hulu Cave, China. Science 294, 2345-2348.

Wolfe, E.W., W.S. Wise, and G.B. Dalrymple, 1997. The geology and petrology of Mauna Kea Volcano, Hawaii: a study of postshield volcanism. U.S. Geological Survey Professional Paper 1557, 129 pp.

Yanase, W., and Abe-Ouchi, A., 2007. The LGM surface climate and atmospheric circulation over East Asia and the North Pacific in the PMIP2 coupled model simulations. Clim. Past 3, 439-451.

Yokochi, B.M., R. Pik, and P. Burnard, 2005. High $^{3}He/^{4}He$ ratios in peridotite xenoliths from SW Japan revisited: Evidence for cosmogenic ^{3}He released by vacuum crushing. Geochem., Geophys., Geosys. 6, doi:10.1029/2004GC000836.

Zhang, R. and T.L. Delworth, 2005. Simulated tropical response to a substantial weakening of the Atlantic thermohaline circulation. Jour. Clim. 18, 1853-1860.

Zreda, M.G. et al., 1991, Cosmogenic chlorine-36 production rates in terrestrial rocks: Earth Planet. Sci. Letters 105, 94-109.

Table 1. Location, geochemical description, and computed ages of samples collected in this study. Wt. crush refers to the weight of mineral crushed and Wt. Melt indicates the melted portion. Ht refers to height of sample above surface. H refers to sample thickness. **Σ** Corr is the combined shielding and boulder geometry corrections from Masarik and Wieler (2003). Due to the open topography of Mauna Kea, the shielding correction was < 1% for all samples. 1 **σ** [^{3}He] uncertainty is analytical uncertainty for the line. Ages and uncertainty were computed using method of Goehring *et al.* (2010). The gray shaded entries are samples that were deemed outliers in the calculation of our mean ages as discussed in the text.

Fig. 1. Location of study area. (**A)** Location of Hawaii in the Central North Pacific. (**B)** Shaded elevation map of the big island of Hawaii with the study area outlined in black **(C)** Geologic map derived from Wolfe et al. (1997) showing the major volcanic and glacial drift units mentioned in the text. Flows are named after their parent cinder cone (triangles). The Wekiu subglacially erupted flow and the Hau Kea synglacially erupted flow have hatching. The Pohakuloa Gulch is the site of the investigation of Blard et al. (2007). Note that the UTM grid provides scale.

Fig. 2. Aerial photographs and associated geologic maps of the two study regions. (**A)** Aerial photo over the Waikahalulu Gulch (lower right of photo) and the MBG moraine (middle left). Bedrock samples were taken from exposures to the left of the cinder cone in the middle right. (**B)** Geologic map of same region showing units relevant to this study. Sample sites are shown with diamonds with the boulder age adjacent. Note that the bedrock samples are from two different flows. (**C)** Aerial photo of the "Cone A" region where two moraine crests and the outwash plain were sampled. (**D)** As in (**B)** but for the Cone A area.

Fig. 3. Paleoshorelines of former lake on eastern flank of Cone A. The lake was dammed by the Cone A M2 moraine, and drained catastrophically by breaching the moraine dam.

Fig. 4. Comparison plot of olivine (Olv) and clinopyroxene (Cpx) ^{3}He ages showing that, within measurement error, the two mineral phases yield identical results. Black squares are samples treated as described in text. White diamonds were subject to crushing to powder indicating little crushing dependent loss of cosmogenic ^{3}He.

Fig. 5. (A) ^{3}He ages for LLGM moraines (MBG as squares and Cone A M1 as diamonds). Boulder mean age denoted by horizontal black line with uncertainty as the dark gray bar. Inset is a "camel" plot showing the probability distribution for all ages as well as the combined PDF. The reduced χ^2 for the entire population and the selected samples are shown along with the associated mean ages and uncertainty. Sample indicated with light grey fill indicates a too-young boulder age thought to result from exhumation. **(B)** ^{3}He ages for the Waikahalulu Gulch moraine. Samples indicated with light gray indicate samples that lie outside the geological error of the remaining samples. **(C)** ^{3}He ages for bedrock samples. Sample indicated in light gray was near the edge of an outcrop and was unusually well-preserved so was likely shielded by now-eroded glacial drift. **(D)** ^{3}He ages for Cone A M2 moraine destabilization event interpreted as coeval with the Younger Dryas. The two youngest and one oldest boulders have been excluded based on boulder size and likelihood of post-glacial excavation (young boulders) and inheritance (older boulder). **(E)** ^{3}He ages from alluvial fan below Cone A M1 and Cone A M2. We tentatively draw mean ages for the potential grouping amongst the older and younger boulders. The older boulders are interpreted to represent activation of the outwash plain during the post-LLGM advance, while younger boulders are interpreted to record reactivation of the outwash

plain in sync with Cone A M2 destabilization. Dashed horizontal lines represent the tentative nature of this interpretation.

Fig. 6. Plot of the relationship between erosion rate, the amount of time prior to the LLGM to reach 10% inheritance (dashed line with black squares, left hand y-axis), and the number of years of ice-free conditions between the LLGM and readvance a given erosion rate corresponds to (solid line with open circles, right hand y-axis). The shaded region displays the results with a plausible range of erosion rates for low-flux glaciers.

Fig. 7. Simulated ice thickness maps (meters) for the LLGM over the SW flank of Mauna Kea using the mass balance estimates derived from **(A)** Blard et al. (2007), **(B)** Hostetler and Clark (2000), **(C)** Pigati et al. (2008), and **(D)** this study. Color scale is in meters. Diamonds are LLGM sample sites. White line demarcates extent of LLGM glacial drift. Grid on map is 2.5 km.

Fig. 8. Simulated ice thickness maps (meters) for the readvance over the SW flank of Mauna Kea using the mass balance estimates derived from **(A)** Blard et al. (2007), **(B)** Pigati et al. (2008), **(C)** this study. Color scale is in meters. Triangles are the Waikahalulu Gulch samples dating the readvance. Circles are locations of bedrock samples. Stars are the samples from the CAM2 moraine. Moraine crests are demarcated by white lines. Grid on map is 2.5 km.

Fig. 9. Paleoclimate records showing that changes in the Atlantic meridional overturning circulation and climate occurred at the same time as colder and wetter intervals on Hawaii during the last deglaciation. (**A**) Record of detrital carbonate (%) in ice-rafted debris from the North Atlantic Ocean, with Heinrich event 1 (H1) identified by peak in detrital carbonate (Bond et al., 1999). (**B**) Records of $^{231}Pa/^{230}Th$ from the northeastern Atlantic (blue) and Bermuda Rise (purple), with increasing ratio indicating decreasing strength of the Atlantic meridional

overturning circulation (McManus et al., 2004; Gherardi et al., 2005). (**C**) $\delta^{18}O$ record of Hulu Cave stalagmite (Wang et al., 2001). (**D**) Record of total organic matter from the Arabian Sea (Schulz et al., 1998). (**E**) Record of organic carbon (%) from the Arabian Sea (Ivanochko et al., 2005). (**F**) Records of mass accumulation rate of biogenic silica from southern East Africa (Johnson et al., 2002). (**G**) $\delta^{18}O$ record from the Sulu Sea (Rosenthal et al., 2003). (**H**) Sea surface temperature record from the South China Sea (Kienast et al., 2006). (**I**) Record of color reflectance of sediments from the Cariaco Basin (Peterson et al., 2000). (**J**) Record of $\delta^{18}O$ of seawater from the East Pacific Warm Pool (Benway et al., 2006). (**K**) Sea surface temperature record from off the Pacific coast of Columbia (Pahnke et al., 2007). (**L**) Sea surface temperature record from the eastern tropical Pacific (Kienast et al., 2006). (**M**) Record of natural gamma radiation from Salar de Uyuni, Bolivia ($20^{o}S$) (Baker et al., 2001). Vertical gray bars represent times of large reduction in the AMOC as suggested by the $^{231}Pa/^{230Th}$ records shown in (**B**). Vertical dash-dot lines indicate the mean ages of moraines identifying times of major deglaciation on Hawaii (see Figure 5 for the uncertainty range about those ages).

Sample	Location	Mnrl.	Wt. Crush (g)	$[^3He]/[^4He]$ Crush	Wt. Melt (g)	$[^3He]/[^4He]$ Melt	$[^3He]/[^4He]$	$[^3He]$ at./g	Ht. (cm)	h (cm)	Σ Corr.	lat.	lon.	alt. (km)	Scaling	Age (kyr)
CK03-1	Cone A M2	Cpx	0.2601	7.99 ± 0.03	0.2316	12.60 ± 0.06	12.60	9.53E+06 ± 2.90E+05	90	1	0.96	19.793	-155.454	3.597	7.040	11.9 ± 1.5
CK03-2	Cone A M2	Cpx	0.2714	7.64 ± 0.05	0.2531	16.58 ± 0.06	16.58	9.76E+06 ± 1.97E+05	0	1	0.96	19.792	-155.454	3.597	7.044	12.2 ± 1.5
CK03-3A	Cone A M2	Cpx	0.1298	7.4 ± 0.3	0.1221	28.5 ± 0.5	28.55	3.93E+06 ± 1.42E+05	60	1	0.96	19.792	-155.454	3.590	6.467	5.4 ± 0.7
CK03-3C	Cone A M2	Cpx	0.2792	7.2 ± 0.1	0.2644	81.1 ± 0.9	81.06	3.76E+06 ± 1.29E+05	60	1	0.96	19.792	-155.454	3.590	6.409	5.2 ± 0.6
CK03-4	Cone A M2	Oli	0.2648	8.3 ± 0.1	0.2564	20.0 ± 0.1	20.03	6.79E+06 ± 1.47E+05	14	4	0.93	19.793	-155.454	3.597	6.877	9.0 ± 1.1
CK03-4	Cone A M2	Cpx	0.2501	8.4 ± 0.2	0.2416	38.3 ± 0.3	38.33	6.24E+06 ± 1.20E+05	14	4	0.93	19.793	-155.454	3.597	6.895	8.3 ± 1.0
AN06-07	Cone A M2	Cpx	0.3000	7.25 ± 0.07	0.2702	28.0 ± 0.3	27.98	1.75E+07 ± 3.73E+05	96	2	0.97	19.794	-155.455	3.605	7.416	20.6 ± 2.5
AN06-08	Cone A M2	Oli	0.3000	7.53 ± 0.08	0.2769	57.1 ± 0.7	57.13	9.00E+06 ± 1.79E+05	37	2	0.97	19.792	-155.454	3.597	6.956	11.3 ± 1.4
AN06-08	Cone A M2	Cpx	0.2303	7.1 ± 0.2	0.2196	362 ± 4	361.53	9.55E+06 ± 6.31E+05	37	2	0.97	19.792	-155.454	3.597	6.956	11.9 ± 1.6
AN06-04	Cone A M1	Oli	0.2651	7.81 ± 0.08	0.2378	41.8 ± 0.5	41.83	1.80E+07 ± 3.53E+05	26	2	0.97	19.794	-155.453	3.595	7.389	21.2 ± 2.6
AN06-04	Cone A M1	Cpx	0.2581	7.14 ± 0.07	0.2500	32.7 ± 0.4	32.69	1.77E+07 ± 3.57E+05	26	2	0.97	19.794	-155.453	3.595	7.371	20.9 ± 2.5
AN06-05	Cone A M1	Cpx	0.2325	8.05 ± 0.08	0.2258	20.8 ± 0.2	20.75	1.33E+07 ± 3.43E+05	69	2	0.97	19.793	-155.453	3.585	7.090	16.3 ± 2.0
CK03-6	Waikahalulu	Cpx	0.2048	7.80 ± 0.05	0.1945	14.3 ± 0.1	14.26	1.14E+07 ± 3.11E+05	0	1	0.96	19.788	-155.469	3.555	6.930	14.5 ± 1.8
CK03-7	Waikahalulu	Oli	0.2734	7.85 ± 0.08	0.2580	13.7 ± 0.1	13.74	9.17E+06 ± 2.68E+05	50	1	0.96	19.788	-155.469	3.550	6.842	11.8 ± 1.4
CK03-7	Waikahalulu	Cpx	0.1893	7.5 ± 0.1	0.1823	66.9 ± 0.7	66.88	9.46E+06 ± 2.03E+05	50	1	0.96	19.788	-155.469	3.550	6.843	12.2 ± 1.5
CK03-08	Waikahalulu	Cpx	0.2825	7.77 ± 0.04	0.2744	12.16 ± 0.06	12.16	6.80E+06 ± 2.16E+05	0	1	0.96	19.792	-155.469	3.550	6.814	8.8 ± 1.1
CK03-10A	Waikahalulu	Oli	0.2728	7.79 ± 0.07	0.2632	25.2 ± 0.2	25.17	1.12E+07 ± 2.06E+05	50	3	0.94	19.787	-155.469	3.545	6.822	14.8 ± 1.8
CK03-10A	Waikahalulu	Cpx	0.2541	7.69 ± 0.08	0.2496	20.0 ± 0.1	20.05	1.06E+07 ± 2.14E+05	50	3	0.94	19.787	-155.469	3.545	6.788	14.2 ± 1.7
AN06-10	Waikahalulu	Oli	0.2821	7.79 ± 0.08	0.2748	13.7 ± 0.2	13.75	8.92E+06 ± 3.25E+05	44	2	0.91	19.787	-155.469	3.535	6.760	12.3 ± 1.5
AN06-11	Waikahalulu	Oli	0.3000	8.12 ± 0.08	0.2689	22.4 ± 0.3	22.36	7.01E+06 ± 1.75E+05	59	2	0.92	19.787	-155.469	3.535	6.729	9.6 ± 1.2
AN06-12	Waikahalulu	Cpx	0.3000	7.42 ± 0.07	0.2483	16.6 ± 0.2	16.59	1.20E+07 ± 3.41E+05	98	2	0.94	19.788	-155.469	3.578	7.006	15.3 ± 1.9
AN06-16A	Waikahalulu	Oli	0.2888	7.77 ± 0.08	0.2797	28.5 ± 0.3	28.53	1.47E+07 ± 3.18E+05	86	2	0.94	19.788	-155.469	3.560	7.138	18.5 ± 2.2
AN06-16A	Waikahalulu	Cpx	0.2821	7.74 ± 0.08	0.2730	102 ± 1	101.68	1.36E+07 ± 2.69E+05	86	2	0.94	19.788	-155.469	3.560	7.079	17.4 ± 2.1
AN06-16B	Waikahalulu	Cpx	0.2873	7.39 ± 0.07	0.2710	15.2 ± 0.2	15.20	1.52E+07 ± 4.67E+05	91	2	0.94	19.788	-155.469	3.560	7.136	19.2 ± 2.4
AN06-17	Waikahalulu	Cpx	0.3000	8.09 ± 0.08	0.2544	42.7 ± 0.5	42.66	1.21E+07 ± 2.41E+05	43	2	0.93	19.788	-155.469	3.550	6.946	15.8 ± 1.9
AN06-18	Waikahalulu	Cpx	0.2310	7.8 ± 0.3	0.2246	41.6 ± 0.5	41.60	1.05E+07 ± 2.14E+05	49	2	0.93	19.787	-155.469	3.540	6.812	14.0 ± 1.7
CK03-13	MBG	Oli	0.1905	8.4 ± 0.2	0.1822	61.0 ± 0.4	60.98	1.92E+07 ± 3.03E+05	40	1	0.96	19.789	-155.480	3.560	7.400	22.9 ± 2.7
CK03-14	MBG	Oli	0.1690	8.64 ± 0.09	0.1605	84.3 ± 0.7	84.29	1.79E+07 ± 3.29E+05	65	5	0.92	19.789	-155.482	3.560	7.223	23.0 ± 2.8
CK03-14	MBG	Cpx	0.2160	8.22 ± 0.04	0.2080	30.5 ± 0.2	30.52	1.75E+07 ± 2.84E+05	65	5	0.92	19.789	-155.482	3.560	7.195	22.5 ± 2.7
CK03-15	MBG	Oli	0.1275	8.8 ± 0.3	0.1184	91.4 ± 0.7	91.43	1.42E+07 ± 3.50E+05	60	1	0.96	19.789	-155.481	3.560	7.137	17.6 ± 2.1
CK03-5	Striated Bedrock	Cpx	0.2597	4.9 ± 0.2	0.2154	216 ± 1	216.41	1.36E+07 ± 4.08E+05	0	1	0.99	19.791	-155.463	3.670	7.509	15.5 ± 1.9
CK03-16	Striated Bedrock	Cpx	0.2256	6.3 ± 0.3	0.2032	137 ± 1	136.58	1.67E+07 ± 3.46E+05	0	3	0.96	19.791	-155.466	3.652	7.503	19.6 ± 2.4
CK03-17	Striated Bedrock	Cpx	0.2781	7.3 ± 0.1	0.2701	112.9 ± 0.8	112.86	1.72E+07 ± 2.75E+05	0	1	0.99	19.791	-155.466	3.652	7.656	19.3 ± 2.3
AN06-19	Striated Bedrock	Cpx	0.2803	7.1 ± 0.2	0.2712	140 ± 2	139.97	9.00E+06 ± 2.43E+05	0	2	0.97	19.793	-155.462	3.670	7.248	10.8 ± 1.3
AN06-20	Striated Bedrock	Cpx	0.2649	6.8 ± 0.2	0.2558	209 ± 3	208.78	1.52E+07 ± 3.91E+05	0	9	0.89	19.795	-155.462	3.690	7.313	19.7 ± 2.4
AN06-22	Lk. Waiau Boulder	Oli	0.3000	7.8 ± 0.1	0.2924	74.5 ± 0.9	74.51	1.58E+07 ± 2.91E+05	0	2	0.94	19.813	-155.477	4.020	9.108	15.7 ± 1.9
CK03-22A	Flood Deposit	Oli	0.2499	7.8 ± 0.2	0.2357	84.6 ± 0.9	84.57	7.73E+06 ± 1.80E+05	35	7.5	0.89	19.789	-155.452	3.499	6.339	11.6 ± 1.4
CK03-22A	Flood Deposit	Cpx	0.2053	8.2 ± 0.1	0.1931	290 ± 3	290.12	7.75E+06 ± 5.70E+05	35	7.5	0.89	19.789	-155.452	3.499	6.339	11.7 ± 1.0
CK03-23	Flood Deposit	Oli	0.2057	8.4 ± 0.3	0.1993	53.1 ± 0.5	53.12	9.75E+06 ± 1.89E+05	55	1	0.96	19.790	-155.452	3.511	6.698	12.8 ± 0.8
CK03-24	Flood Deposit	Oli	0.1085	8.57 ± 0.09	0.0973	15.7 ± 0.1	15.66	1.36E+07 ± 3.89E+05	65	1	0.96	19.791	-155.452	3.536	7.011	17.1 ± 1.1
CK03-24	Flood Deposit	Cpx	0.1664	7.74 ± 0.09	0.1565	32.0 ± 0.2	31.95	1.30E+07 ± 2.25E+05	65	1	0.96	19.791	-155.452	3.536	6.967	16.4 ± 1.0
CK03-25	Flood Deposit	Oli	0.2299	8.20 ± 0.12	0.2212	56.7 ± 0.2	56.68	1.25E+07 ± 1.85E+05	40	3.5	0.93	19.790	-155.452	3.536	6.833	16.6 ± 1.0

Figure 1.

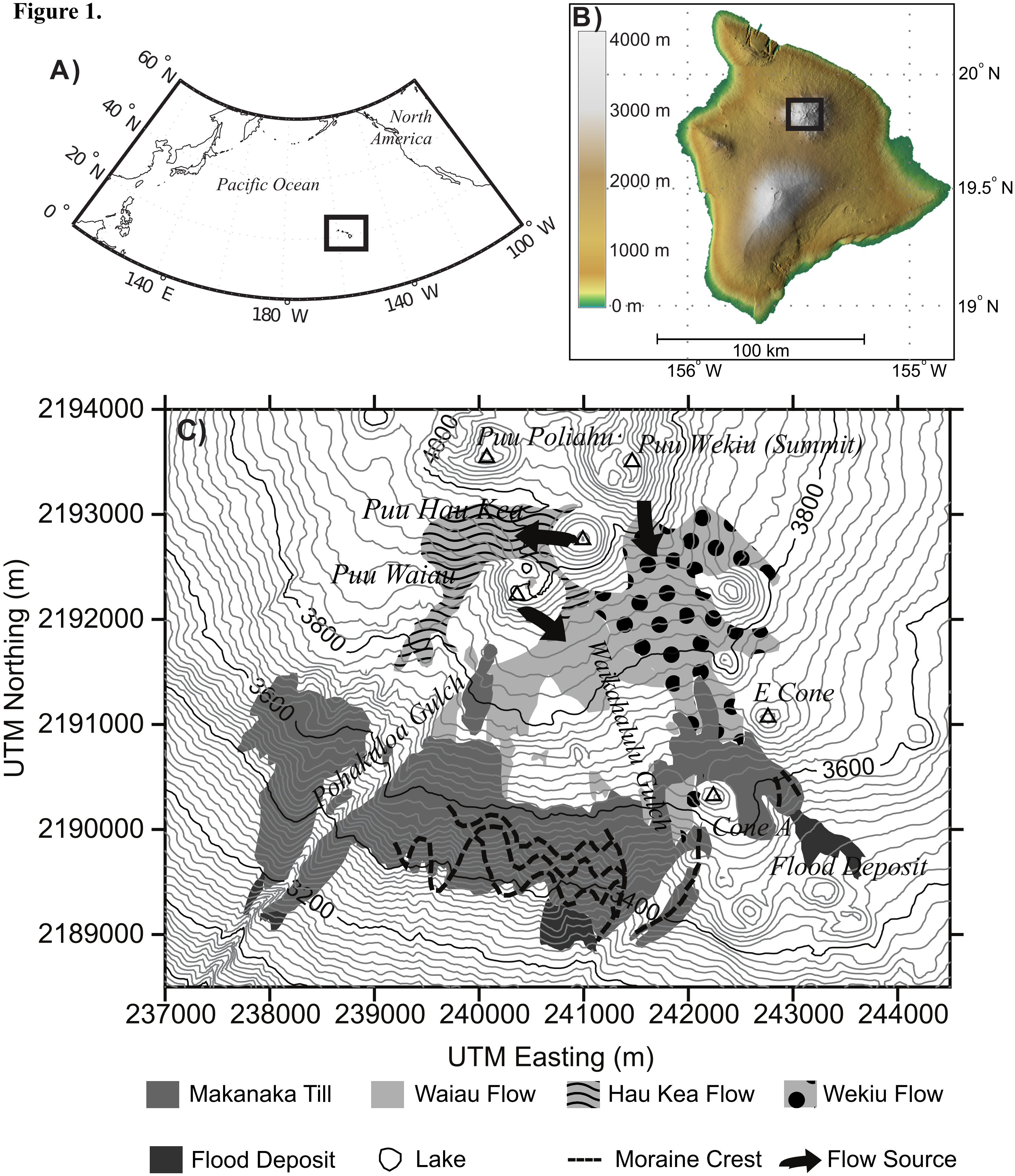

A)
60 °N
40 °N
20 °N
0 °
North America
Pacific Ocean
140 °E
180 °W
140 °W
100 °W
B)
4000 m
3000 m
2000 m
1000 m
0 m
20° N
19.5° N
19° N
100 km
156° W
155° W
C)
Puu Poliahu
Puu Wekiu (Summit)
Puu Hau Kea
Puu Waiau
E Cone
Cone A
Flood Deposit
Pohakuloa Gulch
Waikahalulu Gulch
4000
3800
3600
3400
3200
2194000
2193000
2192000
2191000
2190000
2189000
UTM Northing (m)
237000
238000
239000
240000
241000
242000
243000
244000
UTM Easting (m)
Makanaka Till
Waiau Flow
Hau Kea Flow
Wekiu Flow
Flood Deposit
Lake
Moraine Crest
Flow Source

Figure 2.

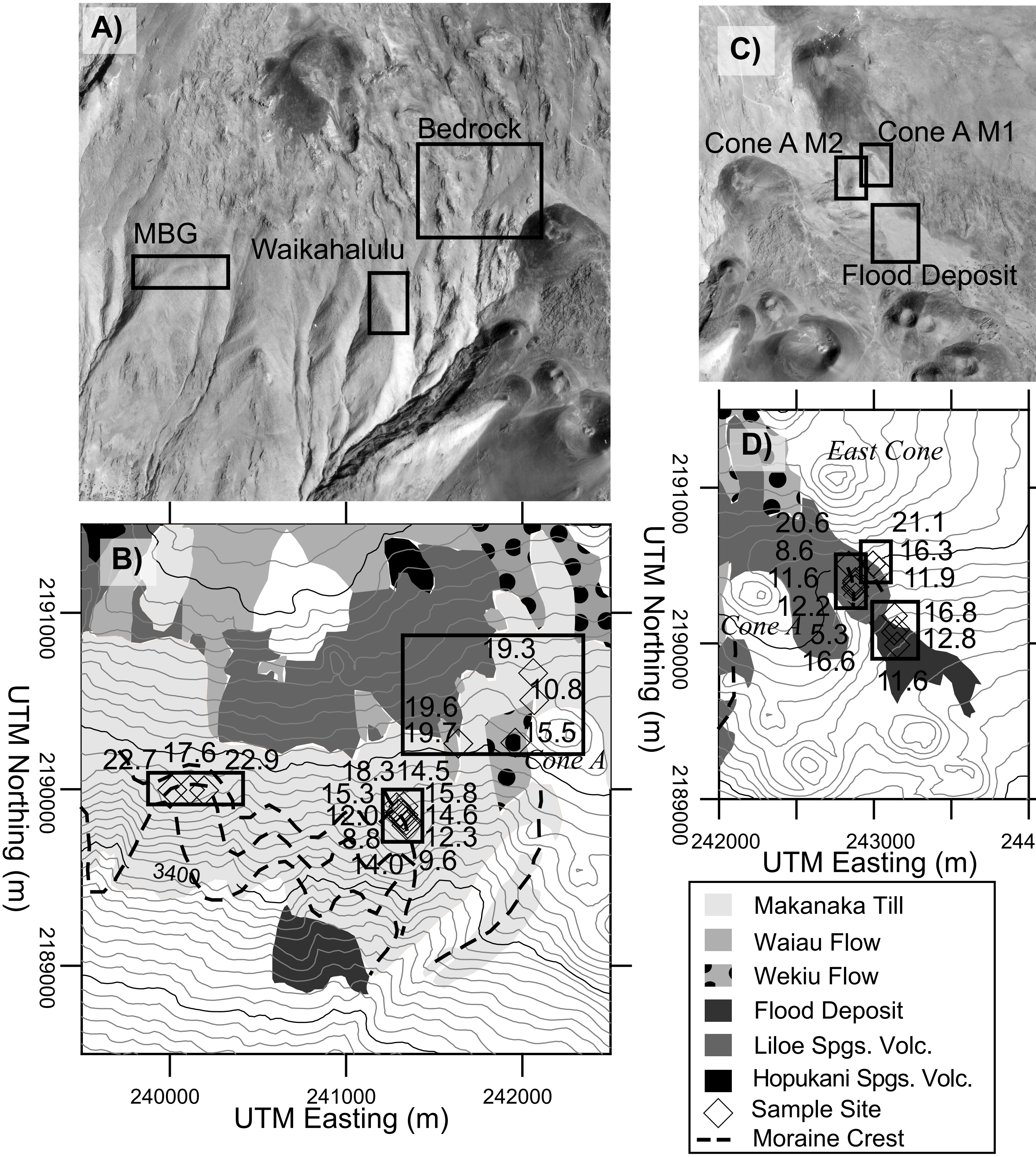

A)
Bedrock
MBG
Waikahalulu
C)
Cone A M2
Cone A M1
Flood Deposit
B)
19.3
10.8
19.6
19.7
15.5
Cone A
22.7
17.6
22.9
18.3
14.5
15.3
15.8
12.0
14.6
8.8
12.3
14.0
9.6
3400
2191000
2190000
2189000
UTM Northing (m)
240000
241000
242000
UTM Easting (m)
D)
East Cone
20.6
21.1
8.6
16.3
11.6
11.9
12.2
16.8
Cone A
5.3
12.8
16.6
11.6
242000
243000
244000
Makanaka Till
Waiau Flow
Wekiu Flow
Flood Deposit
Liloe Spgs. Volc.
Hopukani Spgs. Volc.
Sample Site
Moraine Crest

Figure 3.

Figure 4.

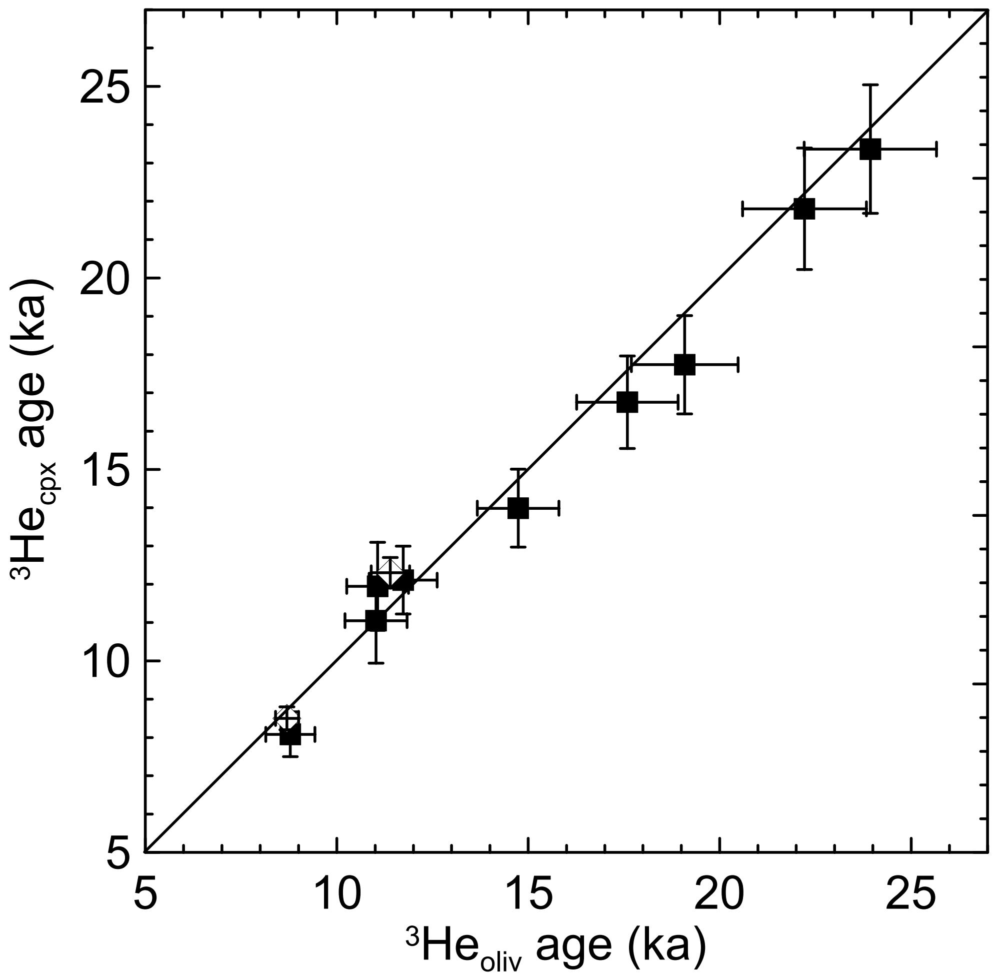

Figure 5.

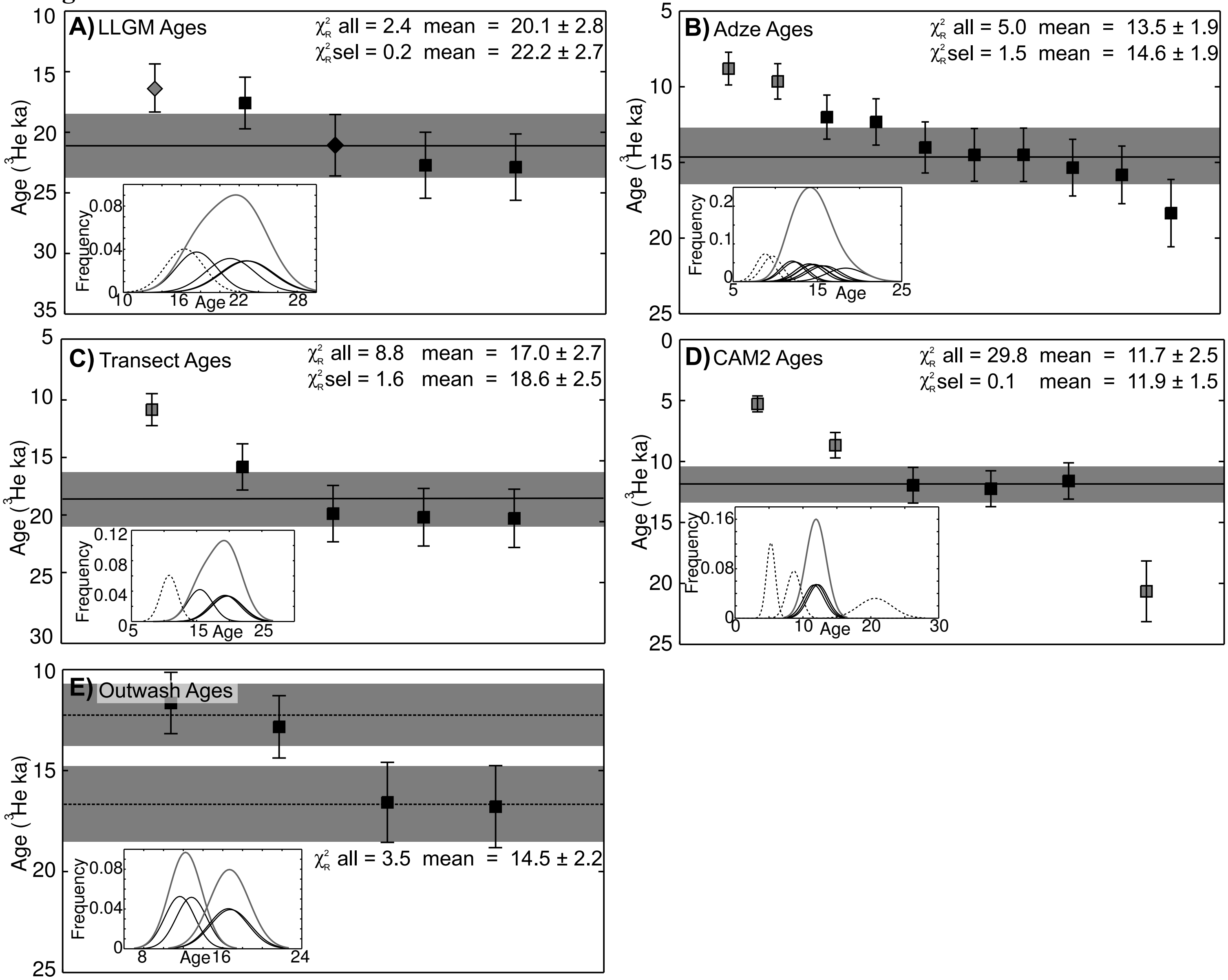
A) LLGM Ages
χ^2_R all = 2.4 mean = 20.1 ± 2.8
χ^2_Rsel = 0.2 mean = 22.2 ± 2.7
Age (^{3}He ka)
Frequency
Age
B) Adze Ages
χ^2_R all = 5.0 mean = 13.5 ± 1.9
χ^2_Rsel = 1.5 mean = 14.6 ± 1.9
Age (^{3}He ka)
Frequency
Age
C) Transect Ages
χ^2_R all = 8.8 mean = 17.0 ± 2.7
χ^2_Rsel = 1.6 mean = 18.6 ± 2.5
Age (^{3}He ka)
Frequency
Age
D) CAM2 Ages
χ^2_R all = 29.8 mean = 11.7 ± 2.5
χ^2_Rsel = 0.1 mean = 11.9 ± 1.5
Age (^{3}He ka)
Frequency
Age
E) Outwash Ages
χ^2_R all = 3.5 mean = 14.5 ± 2.2
Age (^{3}He ka)
Frequency
Age

Figure 6.

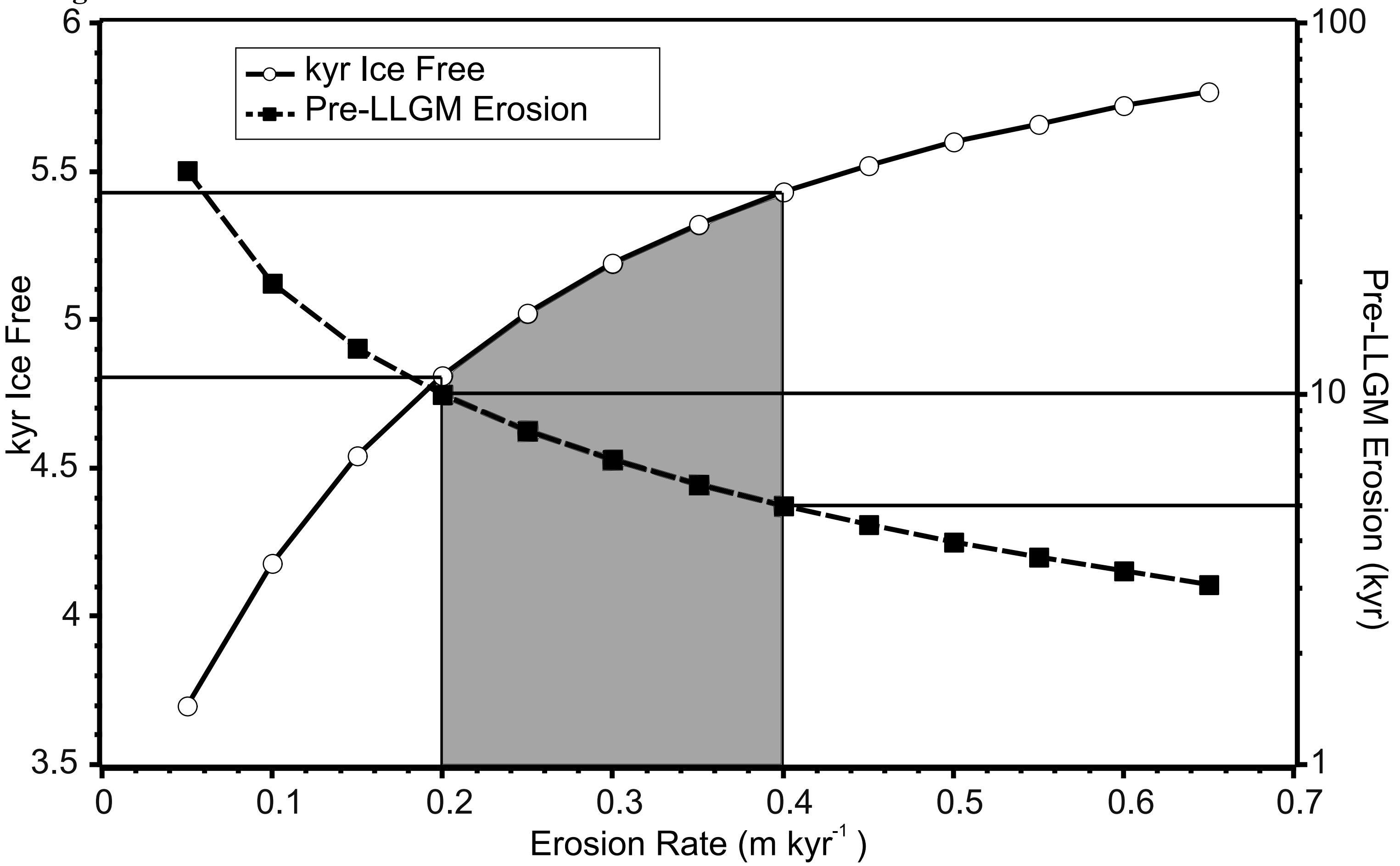
kyr Ice Free
Pre-LLGM Erosion
kyr Ice Free
Pre-LLGM Erosion (kyr)
Erosion Rate (m kyr⁻¹)
6
5.5
5
4.5
4
3.5
100
10
1
0
0.1
0.2
0.3
0.4
0.5
0.6
0.7

Figure 7.

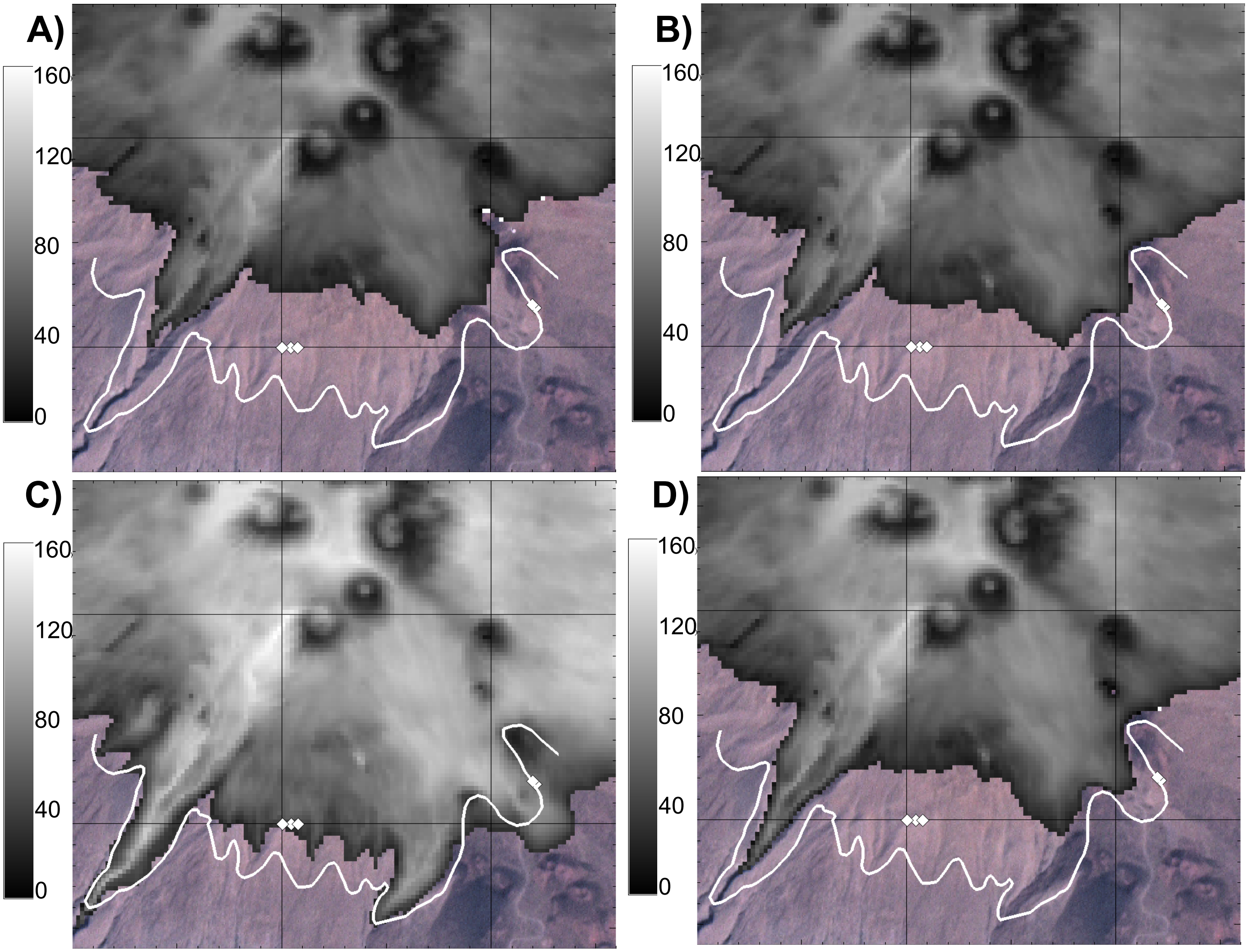

Figure 8.

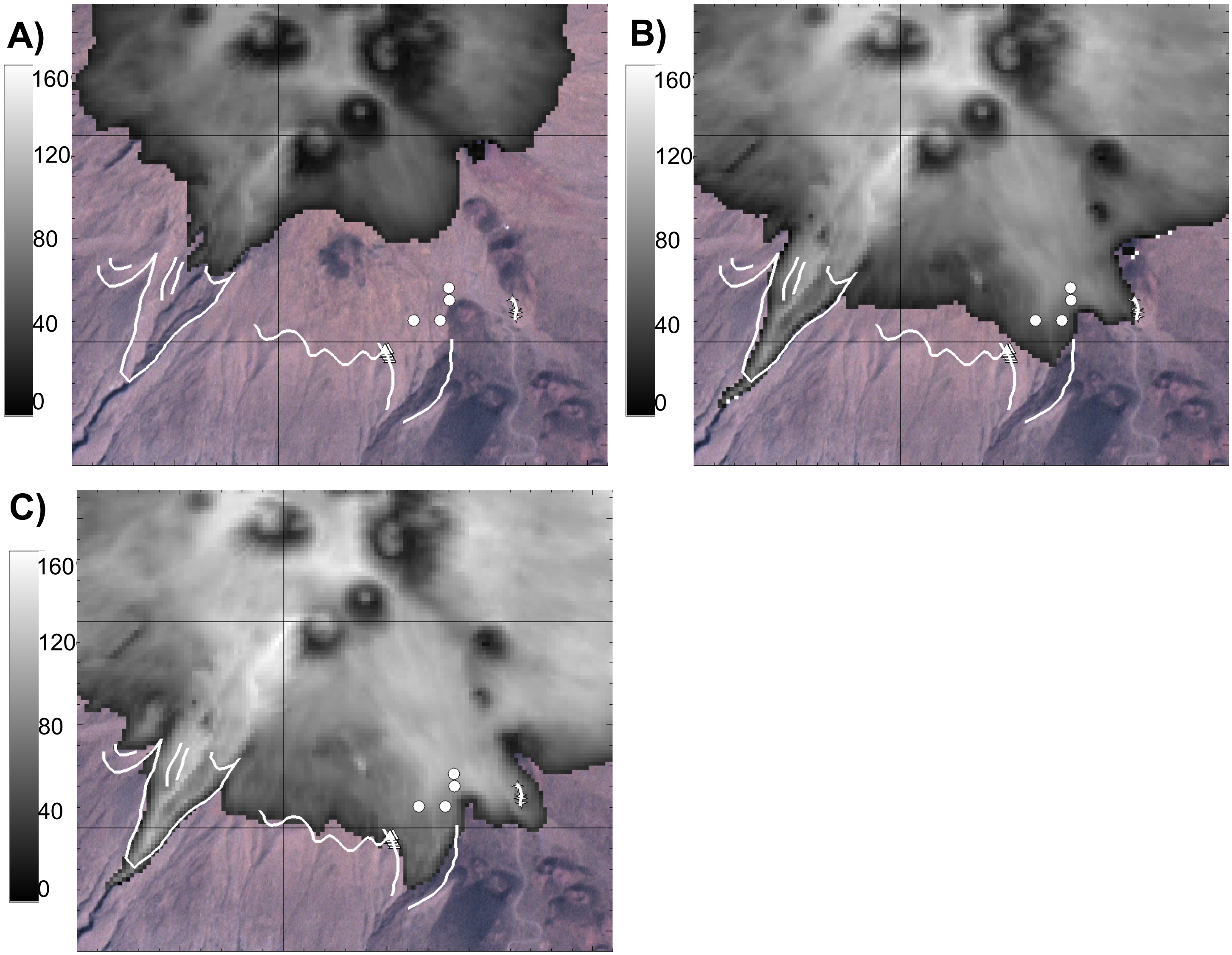

Figure 9.

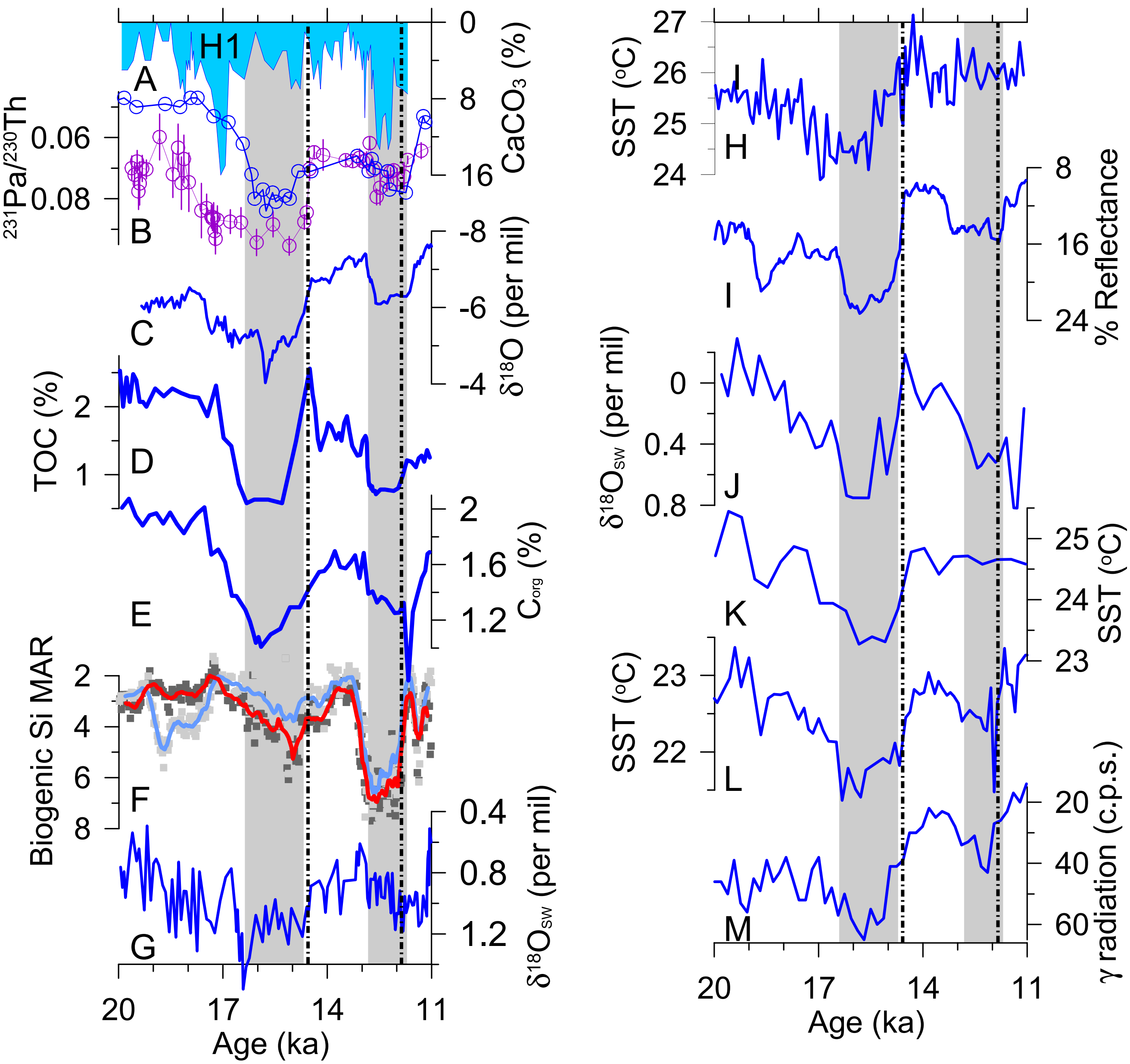

H1
A
B
C
D
E
F
G
H
I
J
K
L
M
CaCO3 (%)
0
8
16
231Pa/230Th
0.06
0.08
δ18O (per mil)
-8
-6
-4
TOC (%)
2
1
Corg (%)
2
1.6
1.2
Biogenic Si MAR
2
4
6
8
δ18Osw (per mil)
0.4
0.8
1.2
20
17
14
11
Age (ka)
SST (oC)
27
26
25
24
% Reflectance
8
16
24
δ18Osw (per mil)
0
0.4
0.8
SST (oC)
25
24
23
SST (oC)
23
22
γ radiation (c.p.s.)
20
40
60
20
17
14
11
Age (ka)

Figure S1.

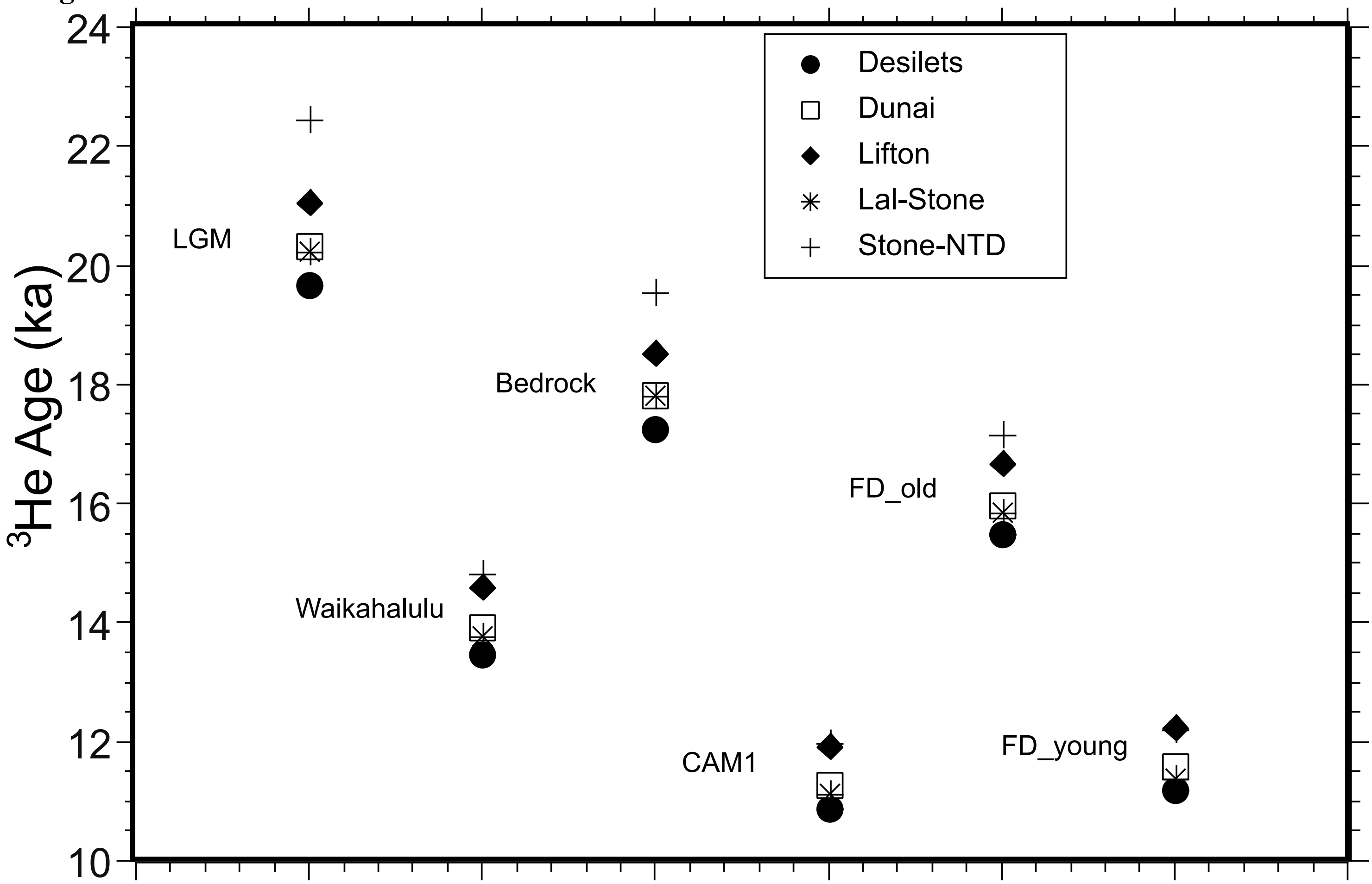

^{3}He Age (ka)
24
22
20
18
16
14
12
10
Desilets
Dunai
Lifton
Lal-Stone
Stone-NTD
LGM
Bedrock
FD_old
Waikahalulu
CAM1
FD_young

Figure S2.

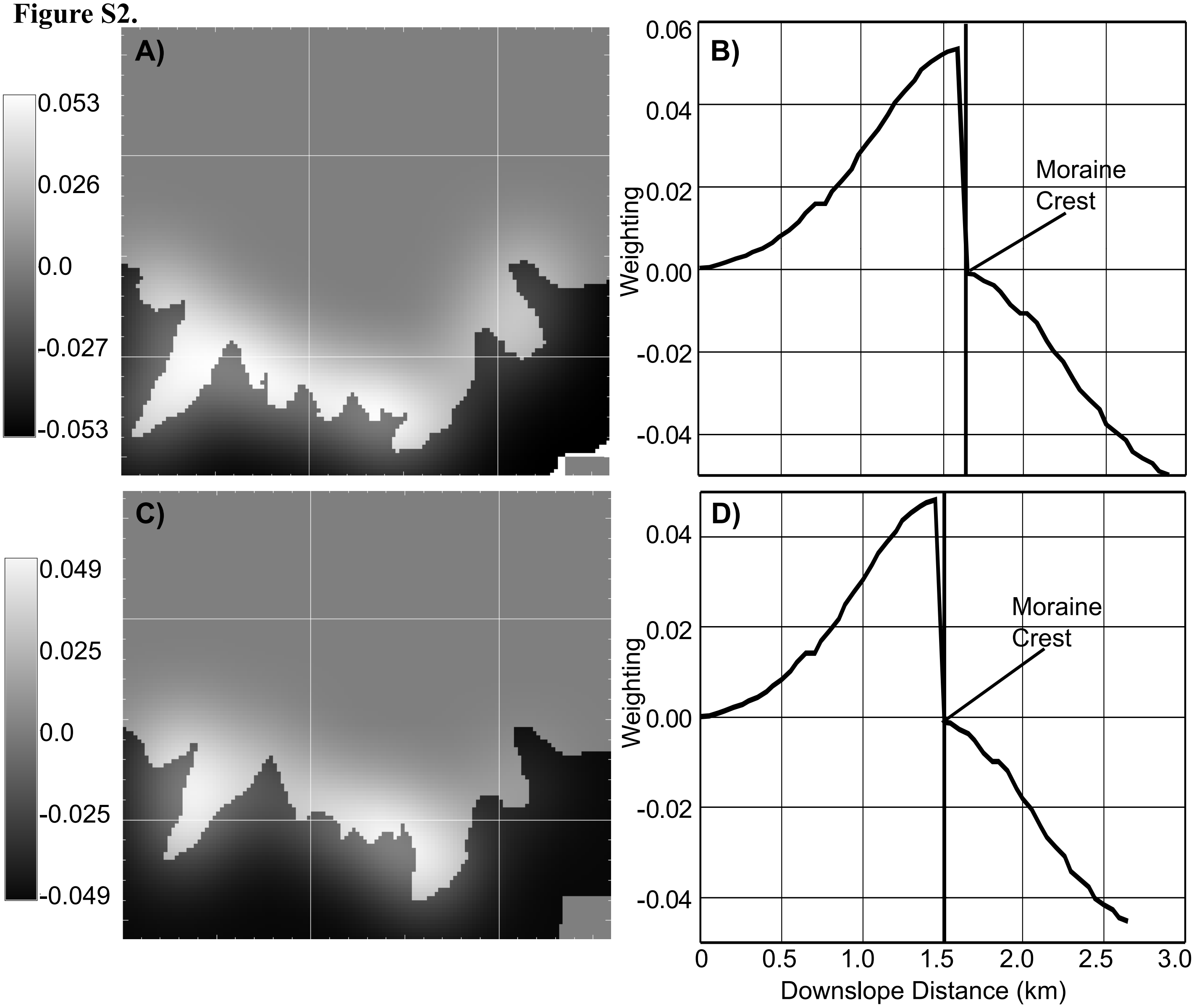
A)
0.053
0.026
0.0
-0.027
-0.053
B)
0.06
0.04
0.02
0.00
-0.02
-0.04
Weighting
Moraine
Crest
C)
0.049
0.025
0.0
-0.025
-0.049
D)
0.04
0.02
0.00
-0.02
-0.04
Weighting
Moraine
Crest
0
0.5
1.0
1.5
2.0
2.5
3.0
Downslope Distance (km)

Figure S3.

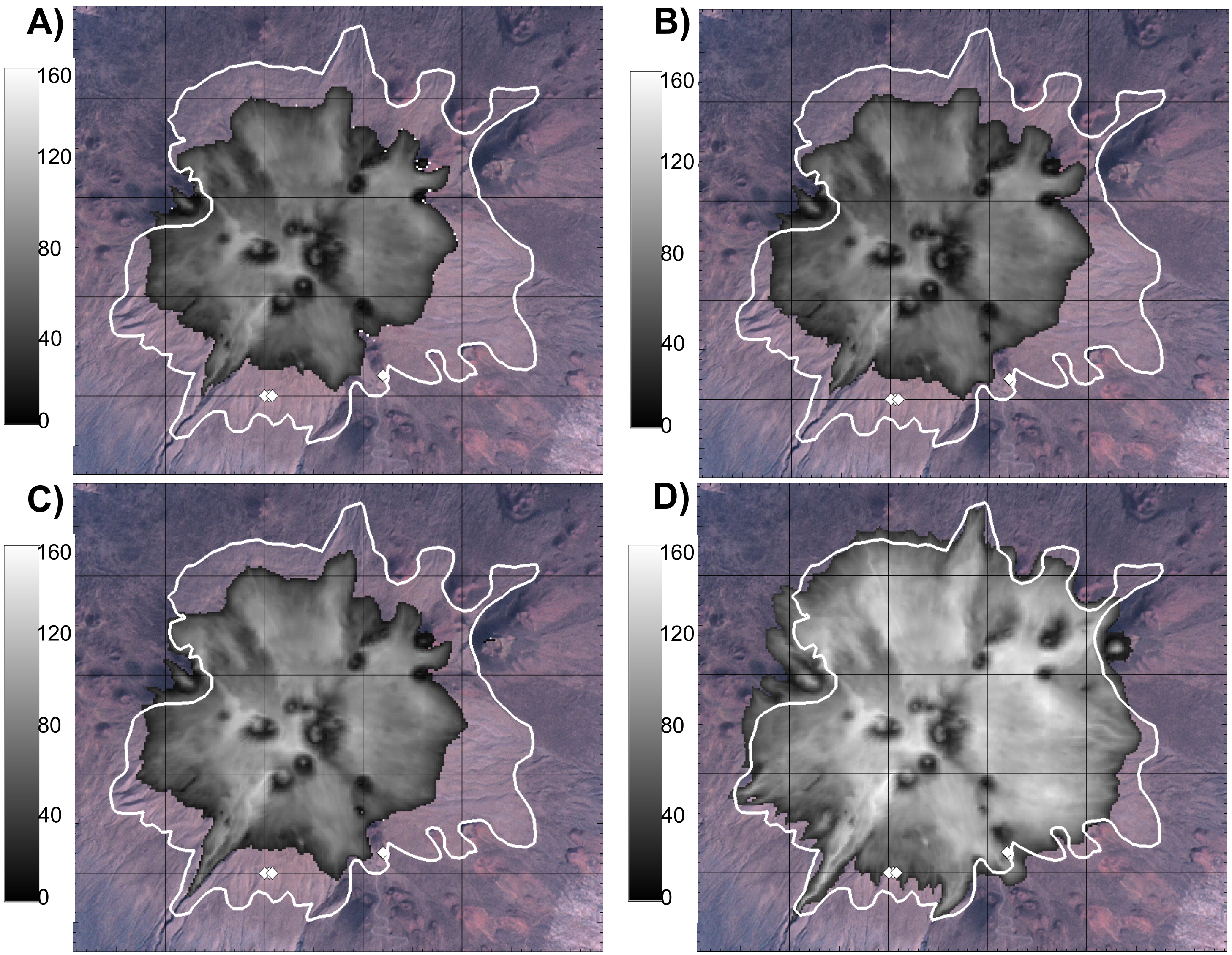

Figure S4.